Satellite-based estimation of contrail cirrus cloud radiative forcing derived through a Rapid Contrail-RF Estimation Approach

Ermioni Dimitropoulou [1], Pierre de Buyl [1], and Nicolas Clerbaux [1]

[1]Royal Meteorological Institute of Belgium, 1180 Brussels, Belgium

Correspondence: Ermioni Dimitropoulou (ermioni.dimitropoulou@meteo.be)

Abstract. ~~Geostationary satellite observations were used to estimate the radiative forcingof~~ Contrails, anthropogenic ice clouds formed by aircraft at cruise altitudes, strongly influence the Earth's radiation budget but the measurement of their radiative forcing (RF) remains poorly quantified at high temporal resolution. In this study, we present the Rapid Contrail-RF Estimation Approach, which uses geostationary satellite observations to estimate their radiative forcing. Starting from a cloud retrieval product, we apply pre-computed Look-Up Tables (LUTs) to generate radiative forcing maps for natural and contrail cirrus clouds~~through a Rapid Contrail-RF Estimation Approach. Meteosat Second Generation/~~ . Specifically, observations from the Spinning Enhanced Visible and InfraRed Imager (~~MSG/SEVIRI) observations were utilized~~ SEVIRI) onboard Meteosat Second Generation (MSG) were used to visually identify days with contrails. For six selected days, ice clouds were characterized using the Optimal Cloud Analysis (OCA) product from MSG/SEVIRI data provided by the European ~~Organisation~~ Organization for the Exploitation of Meteorological Satellites (EUMETSAT). ~~Look-Up Tables (LUTs)~~ The LUTs were constructed using the libRadtran radiative transfer ~~(RT)~~ model to quantify the radiative effect of ice clouds in the ~~shortwave~~ short-wave (SW) and ~~longwave~~ long-wave (LW) spectral regions. ~~The retrieved cloud properties were combined with the LUTs to generate radiative forcing maps for natural and contrail cirrus clouds. A separation scheme isolated the radiative forcing of~~ A cloud top pressure filter was applied to isolate potential contrails. The ~~resulted dataset~~ resulting data set provides a quantification of ~~the~~ SW, LW, and net radiative forcing at the top of the atmosphere ~~(TOA) due to contrails. Over the full diurnal cycle, contrails cause a cooling effect during the daytime and warming at night. The~~ due to potential contrails. We show that these clouds contribute to daytime cooling and nighttime warming, with a net effect that varies between diurnal cycles and seasons. We assess the validity of the Rapid Contrail-RF Estimation Approach ~~'s validity was assessed through correlative~~ through correlation exercises focusing on uncertainties in the use of LUTs, a single ice cloud parameterization, and a calculated cloud top height~~(CTH)~~, supplemented by comparisons with ~~polar-orbiting~~ polar orbiting satellite observations from the Clouds and the Earth~~'~~'s Radiant Energy System (CERES) instruments. ~~Overall~~In general, these correlative comparisons indicate that the proposed approach provides accurate data on ~~contrails radiative forcing estimation~~the estimation of the radiative forcing of potential contrails, with an accuracy ~~on the order~~ of approximately 15 %.

1 Introduction

Understanding the role of clouds in the Earth's radiation budget is crucial for mitigating climate change ~~Wielicki et al. (1995) . The latest IPCC report~~ (Wielicki et al., 1995). The IPCC Sixth Assessment Report (IPCC, 2023) highlights that clouds and aerosols still represent the largest source of uncertainty to estimates and interpretations of the Earth's energy budget, particularly when these clouds are caused by anthropogenic activities such as aviation~~(Lee et al., 2023)~~. Aviation contributes approximately 5% to the anthropogenic climate forcing with the emission of carbon dioxide (CO_2) and non-CO_2 pollutants ~~to be~~ being the two main contributors (Lee et al., 2009, 2021). ~~Since CO_2 emissions are known to be the primary reason of~~ The first effects to be clearly identified and linked to the observed global warming ~~(Letcher, 2020),~~ were those of CO_2 emissions (Letcher, 2020), which is why many studies and reports ~~were focusing primarily~~ initially focused on the quantification of aviation's contribution to the global atmospheric CO_2 concentrations (Olsthoorn, 2001; Pejovic et al., 2008; Ji-Cheng and Yu-Qing, 2012; Mayor and Tol, 2010; Howitt et al., 2011). ~~However, the historical lack of focus on~~ The delayed onset on research of the non-~~CO_2 emissions~~ CO_2 effects is not due to their insignificance for the climate, but rather because ~~they~~ these effects are not yet fully understood and remain associated with considerable uncertainty (Lee et al., 2021).

The non-CO_2 aviation ~~pollutants~~ effects include emissions of pollutants such as nitrogen oxides (NO_x = NO + NO_2), water vapor (H_2O), soot, sulfur oxides (SO_x) ~~and~~ as well as the formation of contrail cirrus clouds (Lee et al., 2021). Among these, ~~contrails~~ contrail cirrus most likely have the largest impact on the TOA radiation budget ~~Burkhardt and Kärcher (2011); Brasseur et al. (201~~ (Burkhardt and Kärcher, 2011; Brasseur et al., 2016). These aviation-induced clouds are formed behind aircraft ~~engines when the mixture of exhaust gases and ambient air arrives in saturation~~ cruising in sufficiently cold air due to the emission of water vapor. If the ambient air is sufficiently humid (that is, the relative humidity with respect to ~~liquid water during the plume expansion (isobaric) process (?). Young~~ ice exceeds 100%), the contrails can persist, as the ice particles within the contrails grow by deposition of water vapor molecules from the ambient air (Schumann, 2005). When newly formed contrails persist and spread into larger clouds, they are called persistent contrails. This occurs when they are formed in ice supersaturated regions (ISSRs) (Schumann et al., 2017; Unterstrasser, 2020). The properties of ~~these young~~ the initial contrails, together with their geometric depth and total ice crystal number, will affect the ~~later~~ properties of the ~~persistent~~ resulting contrail cirrus clouds (Unterstrasser, 2016). The term contrail cirrus is used for the evolution stage of a contrail when it disperses and loses its line-shaped structure. When we use the term contrail on its own, it corresponds to the combination of persistent contrails and contrail cirrus. Only 10-15 % of contrails ~~persist as~~ evolve into contrail cirrus, with an average lifetime of approximately 4 hours (Gierens and Vázquez-Navarro, 2018). ~~These persistent contrails are the only ones relevant for changes in the Earth's radiation budget.~~

The impact of ~~contrails~~ persistent contrails and contrail cirrus on the TOA radiation budget is often quantified using the radiative forcing (RF) ~~metric (Chen et al., 2000) , which~~ (Chen et al., 2000) or the effective RF (ERF) metric. In our case, RF is defined as the ~~change in TOA energy budget due to a constituent in absence of (almost) any other change . In~~ radiative impact of a cloud, calculated as the difference in radiative fluxes at TOA between a cloudy and and cloud-free atmosphere. ERF, in contrast, includes all tropospheric and land surface adjustments, whereas RF only includes the adjustment due to stratospheric

temperature change (Smith et al., 2020). Under most conditions, in the solar wavelength range (i.e., shortwave/SW), ~~contrails have a cooling effect by reflecting incident radiation while in~~ persistent contrails and contrail cirrus reflect incoming sunlight back to space, resulting in a negative radiative effect and thus a cooling influence. In the thermal-infrared wavelength range (i.e~~.~~, longwave/LW), ~~a warming effect by absorbing and emitting radiation. By summing both radiative forcings~~they trap outgoing LW radiation within the Earth-atmosphere system, leading to a positive radiative forcing of LW and an associated warming effect (Heintzenberg and Charlson, 2009). By adding both radiative components, the net radiative effect of ~~cirrus clouds~~ the cirrus clouds and consequently, contrails, can be calculated. This net effect can be either positive or negative, depending on the microphysical, macrophysical and optical properties of the contrail cirrus, as well as the radiative properties of the environment (Wolf et al., 2023). For example, cloud properties such as the cloud optical thickness, cloud temperature, and ice crystal shape influence the net radiative response (Kärcher and Burkhardt, 2013; Stephens et al., 2004; Markowicz and Witek, 2011), while environmental parameters like the surface albedo and surface temperature can play a significant role (Schumann and Mayer, 2017)
~~.~~

The estimation of contrails' RF and/or ~~effective RF (ERF)~~ ERF both globally and regionally over extensive time periods is crucial for understanding aviation's contribution to climate change. On a global scale, either general circulation models of the atmosphere, ~~such as the European Centre/Hamburg general circulation model version 4 (ECHAM4) and the Community Atmosphere Model (CAM5),~~ reanalyses data in combination with radiative transfer ~~modelling~~modeling, or a combination of a model and observations are used to estimate the global yearly mean contrails' net RF and/or ERF (Rädel and Shine, 2008; Lee et al., 2021; Gettelman et al., 2021; Bock and Burkhardt, 2016; Chen and Gettelman, 2013; Bier and Burkhardt, 2022; Teoh et al., 2024). These studies have reported that the presence of contrails has a yearly positive global net radiative impact, which varies significantly between studies, ranging from 6 mW/m^2 (Rädel and Shine, 2008) to 62.1 mW/m^2 (Teoh et al., 2024).

On smaller spatial and temporal scales, ~~whether the net effect of contrails is dominated by cooling (negative RF) or warming (positive RF) is highly dependent on the properties of the contrail, as well as the radiative properties of the environment (Wang et al., 2024; Wolf et al., 2023). To address this, the behavior of contrails over different regions, times of day, and seasons should be investigated. To cover the lifetime of persistent contrails and study their diurnal variation, the use of low earth orbit (LEO) satellites provides observations of high spatial resolution but limited temporal coverage (maximum two overpasses per day over a region) (Spangenberg et al., 2013; Mannstein et al., 1999; Duda et al., 2019). Geostationary satellites, on the other hand, provide high temporal resolution with satellite images available every 15 minutes, as in the case of MSG/SEVIRI observations, while offering high spatial resolution for the portion of the globe they observe. Thus, some studiesuse~~ studies have been carried out using polar-orbiting ~~satellite observations together with geostationary satellite observations, while others rely only on geostationary satellite observations (Haywood et al., 2009; Wang et al., 2024; Dekoutsidis et al., 2023; Duda et al., 2004; Mannste~~ satellite observations, geostationary ones or a combination of both (Haywood et al., 2009; Wang et al., 2024; Dekoutsidis et al., 2023; Duda
. The development of efficient and convenient methods for the observation of RF from contrails is thus necessary to extend the spatial and temporal coverage of their radiative impact studies.

Once the contrails are detected, radiative transfer models can be used to quantify their radiative effect ~~on~~ at the TOA. Although it is not the only way to perform such a task (Haywood et al., 2009), radiative transfer models are a useful tool

to quantify the radiative impact of clouds. In the study of Wang et al. (2024), the quantification of the net effect of ~~contrails~~ contrail cirrus is conducted by performing full radiative transfer calculations with the inputs being the measured cloud and environmental properties for each satellite pixel over Western Europe for two days. It has been proposed by Wolf et al. (2023) that once the cloud and environmental properties are well-described, a large number of RT simulations can be performed ~~to construct cirrus clouds , and contrail cirrus~~ ahead of time to construct ice clouds RF LUTs instead of performing the full radiative transfer calculations for each pixel. By using visible and infrared imagers aboard geostationary satellites, the observation capability of contrails is limited in terms of cloud optical depth (COD). In (Driver et al., 2025), the authors remark on the basis of simulated contrail detection that there is a lower bound of about 0.05 in COD (thinner contrails are not detected). This limitation applies to the detection of contrails but implies that the RF estimates can only be performed on the detected clouds, which misses part of the contrail lifecycle.

The use of RF LUTs combined with geostationary satellite observations offers many advantages but also presents some drawbacks. By performing a large number of radiative transfer simulations once, while varying relevant parameters, such as the solar zenith angle, the surface albedo, the ice cloud's optical thickness, etc., we can construct multi-dimensional LUTs, which describe the behavior of the solar and thermal/~~infra-red~~ infrared RF (RF_{sol} and RF_{tir}, respectively) as a function of these parameters. Then, these LUTs can be merged with geostationary satellite observations to generate contrails ~~'~~ RF maps. Large datasets can be processed relatively quickly, enabling the analysis of full years of geostationary data and the study of daily and seasonal patterns of contrails ~~'~~ RF. Furthermore, once the LUTs are constructed, they are independent of the satellite instrument's characteristics, allowing them to be merged with different satellite observations. However, the primary concern with using LUTs is how accurately they represent the real atmospheric conditions for each pixel. Often, ~~the~~ LUTs are built using standard atmospheric profiles or specific ice cloud properties, which may not capture the variability of real atmospheric conditions.

In this study, a new satellite-based ~~contrails~~ contrail RF maps approach is presented. We refer to this new approach as Rapid Contrail-RF Estimation Approach. A methodological flowchart of the approach is presented in Figure 1. The Rapid Contrail-RF Estimation Approach combines geostationary satellite observations, a cloud properties retrieval algorithm ~~,~~ and radiative transfer modeling~~and a separation scheme between natural and contrail cirrus clouds.~~. In the present work, we use a cloud top pressure filter to separate natural and potential contrail ice clouds. This methodology is not sufficient to discriminate contrails but allows us to validate our RF estimation on ice clouds in general. We discuss the relevance of this limitation and future directions in our conclusions.

First, MSG/SEVIRI observations were employed to visually identify days with the presence of contrails. For the selected days, the detection and characterization of ice clouds, including those overlapping with lower-layer clouds, were performed using the OCA product (EUMETSAT, 2019b) derived from MSG/SEVIRI data. Second, LUTs were constructed using the libRadtran RT model (Emde et al., 2016) to quantify the radiative effects of thin to semi-transparent ice clouds in both the SW (reflected solar radiation) and LW (thermal radiation) spectral regions. Third, the retrieved cloud properties were combined with the LUTs to generate radiative forcing maps of ~~both natural~~ natural cirrus, persistent contrails, and contrail cirrus clouds, with a 15-minute temporal resolution on a regular grid of spatial resolution equal to 0.04^o. Finally, a ~~separation scheme was applied~~

~~to distinguish between natural and contrail cirrus clouds, isolating the radiative forcing specific to contrails~~cloud top pressure separation scheme is used as a substitute for contrail detection. The dataset covers six different days within the 2023-2024 period on a geographic area expanding from 30^oW to 15^oE longitude and 25^oN to 55^oN of latitude. We used the generated RF maps of contrails to investigate their behavior with respect to the TOA radiation budget. The uncertainty of the Rapid Contrail-RF Estimation Approach has been assessed via three different validation exercises by evaluating (1) the choice of using a single atmospheric vertical profile in the RT simulations, (2) the choice of a single ice cloud parameterization scheme, and (3) the impact of using CTH values estimated by a single atmospheric vertical profile on the RF estimations. Additionally, an end-to-end validation is performed by comparing the flux maps for ~~contrails~~ potential contrail cirrus and polar-orbiting satellite observations from the CERES instruments. A comparison between our results and those reported in Wang et al. (2024) for two contrail cirrus outbreaks is also presented.

The paper is organized into five sections: Section 2 ~~presents~~ contains the Rapid Contrail-RF Estimation Approach for generating RF maps for potential contrail cirrus clouds, followed by the necessary data. In Section 3 a description of the methodology for merging the different datasets is provided. The main results of the study, along with ~~four~~ five different validation exercises to assess the validity and estimate the uncertainty of the Rapid Contrail-RF Estimation Approach, are discussed in Section 4. A detailed validation of the Rapid Contrail-RF Estimation Approach is provided in Section 5. Finally, conclusions and future perspectives are ~~provided~~ discussed in Section 6.

2 Data for the Rapid Contrail-RF Estimation Approach

In this study, ~~generating~~ the Rapid Contrail-RF Estimation Approach is deployed to generate RF maps for ~~contrails~~ high-altitude ice clouds above the geographic area of interest~~follows the Rapid Contrail-RF Estimation Approach composed of the initial three steps:~~ , following these three initial steps: (1) detection (Subsection 2.1), (2) characterization (Subsection 2.2), and (3) estimation of the RF (Subsection 2.3) for ~~cirrus clouds~~high-altitude ice-clouds.

Additionally, different datasets have been employed for two main purposes: (1) to accurately describe the conditions and characteristics of the geographic area of interest (see Subsections 2.4 and 2.5) and (2) to validate the RF maps of ~~contrails~~ high-altitude ice-clouds (see Subsections 2.4 and 2.6). A flowchart describing the Rapid Contrail-RF Estimation Approach is ~~shown~~ presented in Figure 1.

2.1 Geostationary Satellite Observations

The detection and characterization of ice clouds was carried out using data from the SEVIRI on board MSG-3 (Meteosat-10) satellite, which is operated by EUMETSAT. MSG-3 is located at 0^o longitude in geostationary orbit, approximately 36.000 kilometres above the Earth's surface ~~.~~

(Schumann et al., 2002). SEVIRI provides spectral information across 11 spectral channels~~covering the visible and infrared spectral regions (Schmetz et al., 2002). These observations are captured every~~ , with a temporal resolution of 15 minutes ~~. The~~ and a spatial resolution of ~~SEVIRI is~~ approximately 3x3 km^2 at the sub-satellite point (SSP) ~~, which can become larger due~~

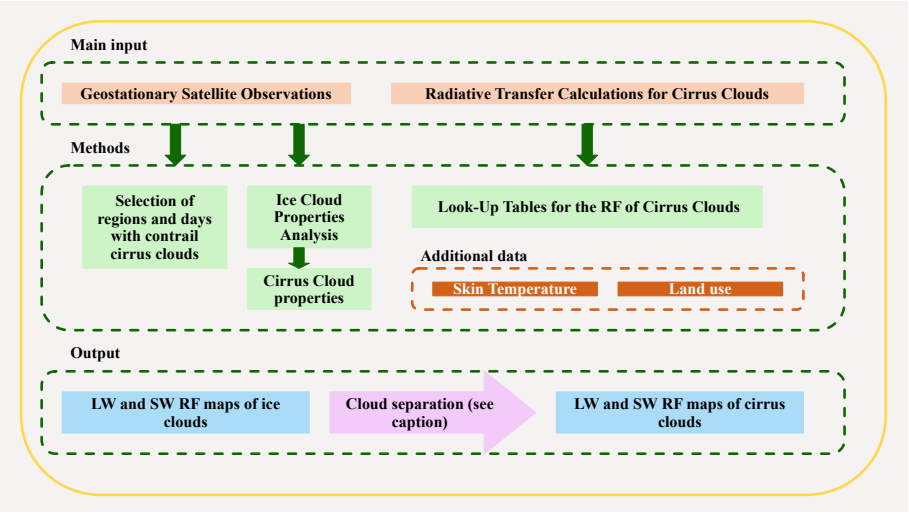

Figure 1. Methodological flowchart describing the Rapid Contrail-RF Estimation Approach. In the present study, the cloud separation scheme is based on a simplified cloud top pressure filter (see Section 3.2)

~~to the satellite's viewing angle. There is an additional channel, the broad-band High-Resolution Visible (HRV), which has a higher spatial resolution compared to the other spectral channels (1x1 km^2), which is not used in cloud retrieval algorithms.~~ (Roberto, 2010; Huckle and Fischer, 2009).

Our primary objective is to investigate the behavior of contrails above different surface types, seasons, and times of the day. These clouds can be visually detected using the Dust/RGB (Red, Green, Blue) composite, which combines data from the MSG/SEVIRI IR8.7, IR10.8 and IR12.0 channels. ~~The Dust product is initially designed to monitor the evolution of dust storms during day and night. Additionally, it is also useful for the detection of thin cirrus clouds.~~ In this product, the contrails appear as long bluish and reddish lines and are visually distinguished ~~by~~ to other cloud types (see Figure 7). Previous studies such as ~~Wang et al. (2023); Schmetz et al. (2002); Dekoutsidis (2019), utilized successfully~~ Wang et al. (2023), Schmetz et al. (2002) , and Dekoutsidis (2019), also successfully utilized the Dust/RGB composite to detect ~~contrail cirrus clouds~~contrails. In this study, using this composite, with the aid of the Satpy Python library (Hoese, 2019) and the EUMETSAT RGB recipes (https://eumetrain.org/manualguides/rgb-recipes), we identified specific days during which we could visually detect geographic regions above Europe and parts of the North Atlantic Ocean where persistent contrails ~~are~~ were present.

In summary, the study area extends from 30^{o}W to 15^{o}E of longitude and 25^{o}N to 55^{o}N of latitude covering data from six different days: 30-01-2023; 13-06-2023; 25-09-2023; 30-01-2024; 17-02-2024; and 28-05-2024. The geostationary grid has been re-projected onto a regular grid with a spatial resolution of 0.04^o.

2.2 Cloud Analysis Product

In the present study, the OCA product is used for the physical characterization of the detected ice clouds.

The OCA algorithm uses the Optimal Estimation (OE) method along with spectral measurements simultaneously to retrieve the cloud state parameters ~~(Rodgers, 2000). The primary concept behind the OE method is to determine the state vector that closely matches the real measurement vector and the simulated measurement vector. A priori information of the atmospheric observations is used together with the forward model to simulate the observations that would be linked to the state vectors. This is done because the problem is ill-posed, which means that more than one state vector can be associated to the observations that we have. Consequently, by using a priori constrains, we select the most likely state which matches the measurements (Rodgers, 2000).~~ (Rodgers, 2000; Mecikalski et al., 2011; EUMETSAT, 2016).

~~Within OCA, the state vector of the retrieval, which describes the state of the atmosphere, contains six variables: the cloud optical thickness (COT), cloud-top particle effective radius (CER), cloud-top pressure (CTP), cloud fraction, cloud phase and surface skin temperature (SST) (Mecikalski et al., 2011). The measurement vector, which is used within OCA, includes the following SEVIRI channels: the reflectance percentage (0 - 1) in the 0.6, 0.8, and 1.6 μm channels and the brightness temperature in the 6.2, 7.3, 8.7, 10.8, 12.0, and 13.4 μm channels. For OCA, the forward model is a radiative transfer model (RTM) and more precisely, LUTs obtained by a fast RTM (FASTRTM). The RTM in the OE method also depends on Numerical Weather Prediction (NWP) data: humidity, temperature and gaseous constituents' profiles, surface albedo and emissivity at the IR channel wavelengths, and other radiative properties (EUMETSAT, 2016).~~

The OCA product is available at a 15-minute frequency and at the full earth scanning area in GRIB format (EUMETSAT, 2019a). It contains single-layer as well as multi-layer cloud situations and the product is structured in layers numbered in a top-down notation: the first layer (named Layer-One) is the highest layer (closest to the top of the atmosphere) and the second layer (named Layer-Two) is the lower layer, which only exists when the pixel has multi-layer cloud conditions (Watts et al., 2011). It should be noted that for the multi-layer cloud scenes, the upper layer is assumed to be an ice cloud and the lower layer a liquid water cloud.

For the present study, we will focus only on pixels characterized as ice or multi-layered clouds (cloud phase) and will use both COT and CTP for the two layers and CER only for the ice cloud. An additional parameter is CTH, which is not included in the OCA product. As we are using a US Standard atmosphere for the construction of the LUTs (see Section 2.3), the same profile has been used to linearly interpolate CTP in the pressure vertical grid, and consequently the altitude vertical grid, of the US Standard atmosphere ~~(Anderson et al., 1986)~~(Anderson et al., 1986). The uncertainty related to the use of a calculated CTH is presented in Section 5.3.

2.3 Radiative Transfer Calculations

LUTs of thin to semi-transparent high-altitude ice clouds are constructed ~~to quantify the contrail cirrus clouds' RF. The simulations are conducted~~ using the libRadtran software (Emde et al., 2016). Apart for the range of the parameters, which should be verified by users of these tables, the method here is applicable to naturally occurring cirrus clouds as well as to contrails. In this work, we perform the validation on all ice clouds that are selected by a cloud top pressure filter.

The libRadtran RT library (version 2.0.5) is used to construct LUTs of TOA irradiances for the SW (reflected solar radiation) and LW (emitted thermal radiation) spectral regions, separately. The RT simulations were performed with the one-dimensional

(1-D) DIScrete ORdinate Radiative Transfer (DISORT) solver (Stamnes et al., 2000), which is included in the libRadtran software package. Using a 1-D solver means that the ice clouds are assumed to be horizontally uniform.

The spectra for both the SW and LW wavelength regions are simulated under three different scene scenarios:

1. Ice cloud above ocean surface,
2. Ice cloud above land surfaces, and
3. Ice cloud above a liquid water cloud.

and, the following input parameters are chosen:

- 16 streams to solve the RT equation, which provides accurate results and limits the computational time.
- a US-standard atmosphere as the main atmospheric profile. The accuracy of such a simplification is assessed in Section 5.1.
- the ice crystal shape to be moderately rough aggregates of eight-element columns based on the ice cloud parameterization of Yang et al. (2013). The uncertainty related to the use of a single ice crystal shape scheme is discussed in Section 5.2.
- the ice water content and effective particle radius to be translated to optical properties based on the ice cloud parameterization of Yang et al. (2013).
- the built-in International Geosphere Biosphere Programme (IGBP) library which is a collection of spectral albedos of different surface types.
- the liquid water content and effective radius of the liquid water cloud to be translated to optical properties based on the parameterization of Hu and Stamnes (1993).

In the SW spectral region, the spectra are simulated from 250 nm up to 5000 nm, while in the LW wavelength region, from 2500 nm up to 98000 nm.

For the LW spectral region and an ice cloud above land and ocean surfaces, the molecular absorption is considered by using the fine resolution REPTRAN parameterization from Gasteiger et al. (2014). For an ice cloud above a liquid water cloud, the same molecular absorption is used but at medium resolution.

Six examples of libRadtran input files (i.e., one in the SW and one in the LW for the three scene scenarios) are provided on the ~~Zenodo~~ Zenodo platform.

The initial output files of the RT simulations in the SW and LW spectral regions contain the wavelength, the output altitude, the direct beam irradiance with respect to the horizontal plane, the diffuse down irradiance and the diffuse up irradiance. These variables are integrated over the total simulation wavelength range separately in the SW and LW wavelength regions to estimate the TOA downward and upward solar/thermal-infrared irradiances (F_{down} and F_{up}, respectively).

RF_{sol} and RF_{tir} of ice clouds are defined as the difference in fluxes between the ice cloud (F_{ic}) and ice cloud-free (F_{icf}) atmosphere at the TOA:

$$RF = F_{ic} - F_{icf} = [F_{down} - F_{up}]_{ic} - [F_{down} - F_{up}]_{icf} \quad (1)$$

Then, the net RF is a summation between RF_{sol} and RF_{tir} (Wolf et al., 2023). It should be noted that negative RF values indicate cooling, while positive ones correspond to warming.

In the SW wavelength range, the LUTs store the TOA F_{down}, F_{up}, and RF_{sol} as a function of the following parameters:

- the Solar Zenith Angle (SZA), COT and CER for an ice cloud above ocean surface,
- the SZA, COT, CER and underlying surface type as defined by the IGBP for an ice cloud above land surface, and
- the SZA, COT, CER and liquid water Cloud Optical Thickness (wCOT) for an ice above a liquid water cloud.

while keeping ~~constant the following~~ the following constant:

- the CTH equal to 10km for the three scene scenarios,
- the ocean Bidirectional Reflectance Distribution Function (BRDF) determined by a wind speed equal to 5 m/s for an ice cloud above ocean surface from Cox and Munk (1954a, b),
- the water Cloud Top Height (wCTH) equal to 3km for an ice cloud above a liquid water cloud.

The LUTs in the LW store the TOA F_{down}, F_{up}, and RF_{tir} by varying the following parameters:

- the SST, CTH, COT, and CER for an ice cloud above ocean surface,
- the underlying LST, CTH, COT, CER and IGBP surface type for an ice cloud above land surface,
- the wCOT, wCTH, CTH, COT, and CER for an ice cloud above a liquid water cloud.

To save computational time, RT simulations have been performed for all IGBP surface types in the SW spectrum but not in the LW spectrum. In the SW spectrum, there are 17 different LUTs, each corresponding to simulations for the 17 different IGBP surface types. The only IGBP surface type not included in these simulations is type 17 (ocean water). For this type, the LUTs correspond to the scenario of an ice cloud above an ocean surface. In the LW, RT simulations were conducted for 8 specific IGBP surface types (i.e., evergreen needle forest, closed shrubs, open shrubs, woody savanna, grassland, urban, antarctic snow, and desert). The other IGBP surface types were mapped to the existing ones based on their similar or closely related emissivity responses.

The LUTs are all stored in a single NetCDF file and are available on the ~~Zenodo~~ Zenodo platform.

The reader should note that the RF values stored in the different LUTs depend on at least three parameters (e.g., SW wavelength range and the scene scenario of ice cloud above ocean) and up to five parameters (e.g., LW wavelength range and the scene scenario of ice cloud above a liquid water cloud). It is complex to illustrate every single dependency of RF with respect to each input parameter. Therefore, we have chosen to demonstrate some of these dependencies in Figures 2 and 3.

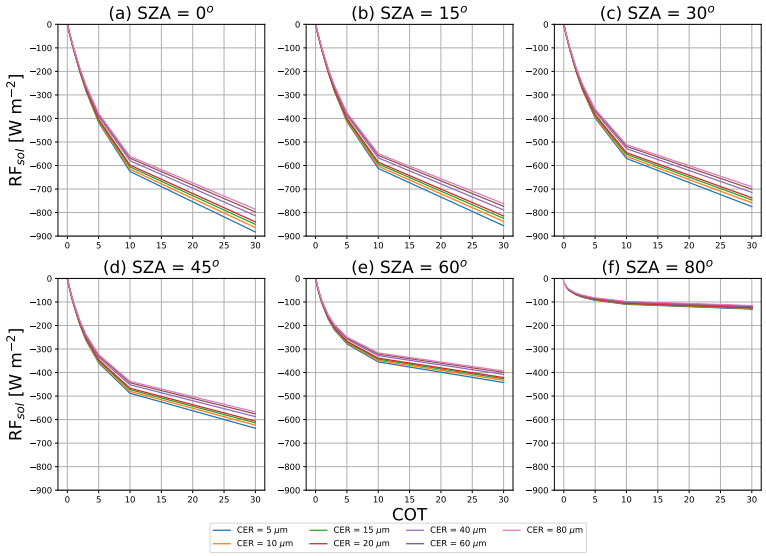

Figure 2. Radiative forcing (RF) in the shortwave (SW) wavelength range (RF_{sol}) as a function of the cloud optical thickness (COT) for different values of ice crystal effective radius (CER) for an ice cloud over the ocean ~~shown~~ presented for six different solar zenith angle (SZA) values ranging from ~~(a)~~ (a) 0^o to ~~(b)~~ (b) 80^o.

Figure 2 ~~shows~~ presents an example of the variation of RF_{sol} for an ice cloud above ocean as a function of COT, SZA (different plots), and CER (different lines in every plot). In the SW wavelength range, RF is negative, corresponding to a cooling effect of the climate at the TOA due to cloud reflectivity. As observed, RF_{sol} increases in magnitude as the ice cloud becomes optically thicker (larger COT values). Additionally, the size of the ice crystals (i.e., CER) becomes significant for optically thick clouds. Finally, as we can see, the SZA also plays an important role in the simulations, resulting in larger absolute RF_{sol} values for a SZA value equal to 0^o.

Similar to Figure 2, Figure 3 ~~shows~~ demonstrates the variation of RF_{tir} for an ice cloud above the ocean as a function of COT, SST (different plots), and CER (different lines in every plot). Here, we observe that RF_{tir} changes rapidly for small values of COT, specifically in the range from 0 to 10. However, RF_{tir} saturates when the cloud reaches a certain optical thickness (approximately a COT equal to 10). The influence of SST on the RF increases as the cloud becomes optically thicker. Additionally, when SST and COT increases, and consequently the infra-red radiation is trapped between surface and ice cloud, RF_{tir} becomes larger. Finally, CER does not have as large ~~as an effect on RF_{tir}~~ an effect as it does on RF_{tir} in the SW wavelength range.

Table 1 provides a summary of all the parameter used in RT simulations with their respective symbol, unit, and range of values.

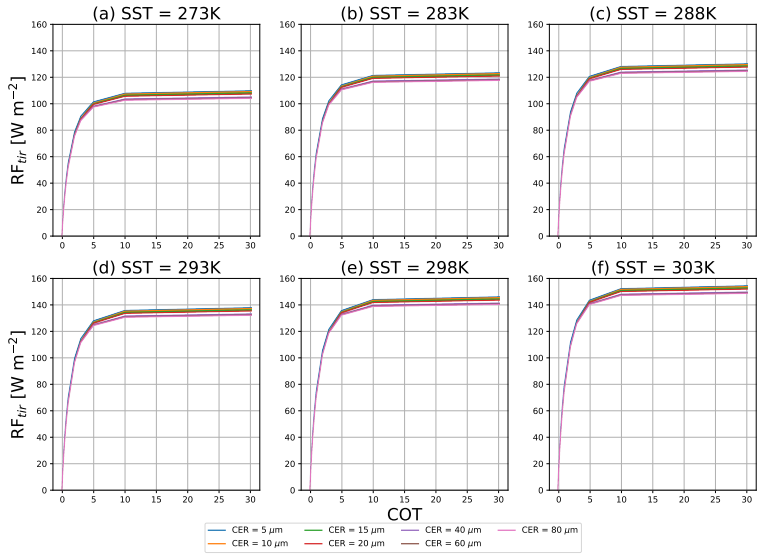

Figure 3. Radiative forcing (RF) in the longwave (LW) wavelength range (RF_{tir}) as a function of the cloud optical thickness (COT) for different values of ice crystal effective radius (CER) for an ice cloud over the ocean ~~shown~~ presented for six different sea surface temperature (SST) values ranging from ~~(a)~~ (a) 273K to ~~(f)~~ (f) 303K. For visual clarity, the SST value equal to 278K is not ~~shown~~ presented here.

2.4 Surface temperature and vertical temperature profiles

As will be seen in Section 3.1, an important input for the LW RT simulations is the surface temperature, called skin temperature (SKT), in the geographic area of interest for each selected day. ~~SKT is defined as a radiative temperature of the model surface.~~ SKT maps are downloaded from the Meteorological Archival and Retrieval System (MARS) archive for the forecast stream (fc) of the European Center for Medium-Range Weather Forecasts (ECMWF) for the six selected days. The data are re-gridded on a regular grid with a spatial resolution equal to 0.04^o, covering the geographic domain of this study (see Figure 4). The data are based on the 00:00:00 UTC and 12:00:00 UTC analysis, each covering the subsequent 12-hour forecast period in a time resolution of one hour. For MSG/SEVIRI observations falling between two time steps, linear interpolation is performed between the two successive time steps to assign SKT maps to those observations.

To assess the validity of using a single atmospheric vertical temperature profile, radiative transfer simulations were performed for selected pixels by using real vertical temperature profiles instead of the LUTs in a number of randomly selected pixels (see Section 5.1). For this purpose, we downloaded hourly ERA5 vertical temperature profiles from the ECMWF's MARS archive for the analysis stream re-gridded onto a regular grid with a spatial resolution of 0.04^o. ~~The profiles are provided in model levels, which are 137 in total. We computed the pressure on these model levels and then, the geopotential height.~~ The temperature profiles are temporally interpolated into the MSG/SEVIRI observation time by using linear interpolation between the analysis data at the previous and next hour.

Table 1. Parameter values used in the SW and LW radiative transfer model (RTM) simulations.

Parameter	Symbol	Wavelength range	Units	Values
Ice cloud optical thickness	COT	SW/LW	1	0, 0.1, 0.2, 0.3, 0.4, 0.5, 0.7, 1.0, 2.0, 3.0, 5.0, 10.0, 30.0
Solar zenith angle	SZA	SW	degrees	0, 5, 10, 15, 20, 25, 30, 35, 40, 45, 50, 55, 60, 65, 70, 75, 80
Ice crystal effective radius	CER	SW/LW	μm	5, 10, 15, 20, 40 , 60, 80
Ice cloud top height	CTH	LW	km	6, 7, 8, 9, 10, 11, 12, 13
Sea surface temperature	SST	LW	K	273, 278, 283, 288, 293, 298, 303
Land surface temperature	LST	LW	K	263, 268, 273, 278, 283, 288, 293, 298, 303, 308, 313
~~Water~~ Liquid water cloud optical thickness	wCOT	SW/LW	1	0.1, 0.5, 1.0, 5.0, 30.0
~~Water~~ Liquid water cloud top height	wCTH	LW	km	1, 2, 3, 4, 5

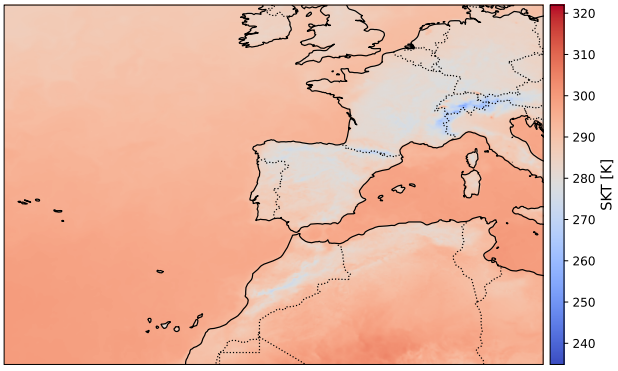

Figure 4. Skin temperature (SKT) map for an example date and observation time (25th of September 2023 and 06:00:00 UTC) over the study area.

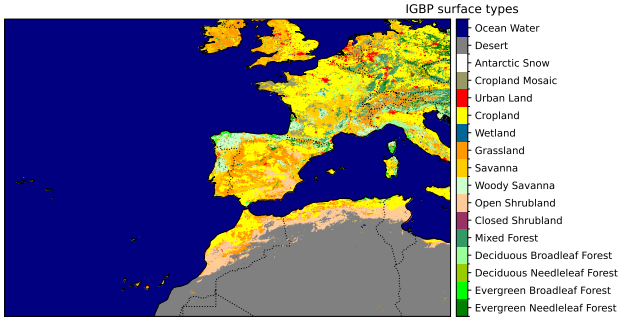

Figure 5. International Geosphere Biosphere Programme (IGBP) land use classification scheme in the selected geographic domain of this study from the MCD12Q1 Version 6.1 data product.

2.5 Land use

Using a representative land use dataset for the geographic area of interest is essential because it affects the RT simulations in the LW wavelength range through the surface aldedo and emissivity. We utilize the Terra and Aqua combined Moderate-Resolution Imaging Spectroradiometer (MODIS) Land Cover Type (MCD12Q1) Version 6.1 data for the most recent available year, 2022. ~~This data product provides global land cover types at yearly intervals derived from MODIS Terra and Aqua reflectance data observations.~~ The MCD12Q1 data are provided as tiles approximately $1000\text{x}1000km^2$ using a sinusoidal grid. ~~In total, there are 460 tiles covering the entire globe.~~ The data are re-projected on a regular grid with a spatial resolution of 0.04^o in the geographic domain of interest (see Fig. 5) with the aid of Satpy Python library (Hoese, 2019).

In this study, we employ the IGBP global vegetation classification scheme, which identifies 17 different land cover classes. It should be noted that in the case of pixels being covered by multiple IGBP classes, we assign the land cover value with the largest percentage coverage to that pixel, with a special treatment for water. We first discriminate whether the pixel is covered by water for more than half of its fine-scale MODIS pixels, in which case it is assigned the water class. Else, we consider all non-water classes for the majority choice.

2.6 Polar Orbiting Satellite Observations

The CERES instruments aboard Terra measure the Earths' total radiation budget (Barkstrom, 1999). This type of satellite observations are essential for assessing the radiative effect of clouds.

The Single Scan Footprint (SSF) TOA/Surface Fluxes and Clouds product contains instantaneous CERES observations for a single scanner instrument (NASA, 2019). The data used in this study combine CERES observations with scene and cloud properties from MODIS on Terra and Aqua satellite. ~~As the footprint of CERES (approximately 20 km) is larger than that of MODIS, the scene identification and cloud properties are averaged over the CERES footprint.~~

In this study, we use TOA SW and LW fluxes from CERES Terra- Flight Model 1 (FM1) and Aqua FM3 Edition 4A SSF to validate the TOA SW and LW flux maps of ~~contrails~~ high-altitude ice-clouds derived using the Rapid Contrail-RF Estimation Approach (see Subsection 5).

3 Methodology of the Rapid Contrail-RF Estimation Approach

Here, we present the methodology followed, first to merge the three principal datasets introduced in Section 2 with the necessary additional data, and finally, to separate potential contrails from natural cirrus clouds (Subsection 3.2).

3.1 Merging the principal datasets

~~RF maps of contrails are generated by merging three principal datasets together with additional data.~~

First, as described in Section 2.1, we use the MSG/SEVIRI Dust/RGB composite to identify specific days during which persistent contrails could be visually detected. It should be noted that contrails with COT values lower than 0.05 are undetectable when using imaging instruments aboard geostationary satellites (Kärcher et al., 2009; Driver et al., 2025). For these particular days, the OCA product is re-gridded onto a regular grid with a spatial resolution equal to 0.04^o, covering the study area, which expands from 30^oW to 15^oE longitude and 25^oN to 55^oN latitude. The necessary additional data, including SKT data (see Section 2.4) and the surface type (see Section 2.5), are also resampled onto the same regular grid with the same spatial resolution as the re-gridded OCA product. As a result, the generated maps contain pixels with information on the cloud phase (cloud-free, liquid, ice, or multi-layered clouds), CTP, COT, CER, SKT, and surface type.

For each pixel characterized as an ice or multi-layered cloud, we first determine which LUT should be used among the three scene scenarios by utilizing the surface type information (land or ocean) and the OCA cloud phase (ice or multi-layered). Once the choice of LUT is made, a multi-dimensional interpolation of the simulated RF_{sol} and RF_{tir} values from the LUT at the actual values of the cloud and environmental parameters for each pixel (SZA, COT, SKT etc.) is performed.

The dimensions of the interpolation are determined by the number of parameters on which RF_{sol} and RF_{tir} depend in each LUT. For instance, for an ice cloud above ocean and within the SW wavelength range, a 3-dimensional interpolation is performed with the simulated RF_{sol} being a function of COT, CER, and SZA parameters. For the same scene within the LW wavelength range, a 4-dimensional interpolation is necessary, where simulated RF_{tir} is a function of COT, SST, CTH, and CER parameters.

The final output of this approach is the construction of RF_{sol} and RF_{tir}, as well as F_{sol} and F_{tir} maps of the detected ice clouds.

3.2 Distinguishing ~~natural~~ between ice and ~~contrail~~ cirrus clouds

Merging the different datasets, as explained in Section 3.1, will generate RF and fluxes maps of both natural and ~~contrail cirrus~~ aviation-induced clouds. To ~~effectively distinguish them~~emulate the detection of persistent contrails, among naturally occurring

Table 2. Selected days, and the geographic limits of each zoomed regions within the geographic area of interest where persistent contrails were visually detected.

Day	Longitude range	Latitude range
30-01-2023	[30^{o}W, 5^{o}W]	[30^{o}N, 55^{o}N]
13-06-2023	[20^{o}W, 10^{o}W]	[25^{o}N, 40^{o}N]
25-09-2023	[10^{o}W, 10^{o}E]	[35^{o}N, 55^{o}N]
30-01-2024	[5^{o}W, 15^{o}E]	[30^{o}N, 45^{o}N]
17-02-2024	[30^{o}W, 5^{o}E]	[30^{o}N, 55^{o}N]
28-05-2024	[10^{o}W, 10^{o}E]	[35^{o}N, 55^{o}N]

and contrail clouds, we apply a filtering method based on the ice clouds' CTP value similar to the approach described in Wang et al. (2024). This procedure does not allow for an impact study of aviation but is sufficient to validate our method.

The rationale behind this approach is that most of commercial airplanes fly at altitudes ranging from 8 to 12 km, which corresponds to a mean pressure level of 250 hPa. However, for a persistent contrail or a contrail cirrus to form, specific atmospheric conditions are required, mainly the presence of an ISSR. ~~In~~ On average, these ISSRs are typically found at slightly higher pressure levels, around 300 hPa. Combining both information, we implement a CTP filter at 300 hPa in our analysis, meaning that clouds above 300 hPa are considered to be ~~contrails~~persistent contrails or contrail cirrus. It should be ~~note~~ noted that this approach provides a rough and approximate filtering compared to better approaches, such as manually labeling remote sensing images (Meijer et al., 2022), or contrail detection algorithms based on machine learning (Ortiz et al., 2024).

4 Results

In this Section, we first present the main results of the study (Subsection 4.1 and 4.2) including the detection and characterization of potential contrails as well as their RF. ~~This is followed by four different validation exercises to assess the performance of the Rapid Contrail-RF Estimation Approach in generating realistic RF maps for contrails (Subsection 5).~~

4.1 Detection and characterization of contrails

The detection and characterization of contrails are conducted for each selected day by zooming on smaller geographic regions within our spatial domain of interest, based on the presence of a large number of contrails. This choice significantly reduces the computational time for Sections 5.1, 5.3, and 5.4, while allowing us to sample pixels over land or ocean on the different days. Figure 6 ~~shows~~ presents the selected longitude and latitude ranges for each day, while Table 2 provides a summary.

Figure 7 ~~shows~~ presents an example of the DUST/RGB composite from SEVIRI/MSG, focusing on the geographic region over France and the Bay of Biscay for September 25th, 2023, from 06:00:00 UTC to 07:15:00 UTC. It should be noted that, for the sake of visual clarity, Figures 7, 8, and 9 demonstrate only a part of the zoomed geographic region where contrails

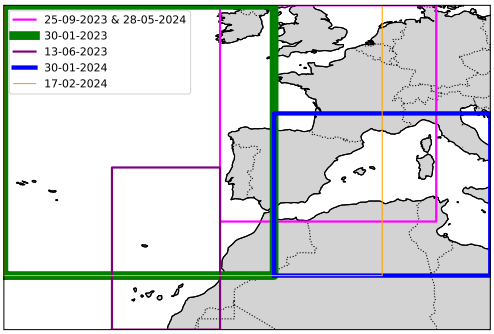

Figure 6. Geographic map of the overall geographic region, illustrating different colored boxes that represent the zoomed geographic areas of interest per day.

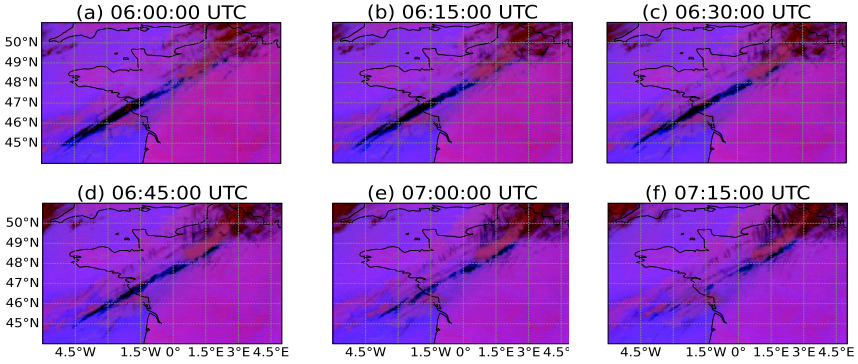

Figure 7. MSG/SEVIRI Dust/RGB images for an example date and sequence of observation times (25th September 2023) in a zoomed geographic area, where contrails are detected.

are observed. At 06:00:00 UTC, a dense ice cloud is observed, surrounded by line-shaped ice clouds over the northern Bay of Biscay and France. As time progresses, the dense ice cloud mass disperses, while at the same time, we observe the formation of several line-shaped ice clouds around it.

As it is ~~shown~~ demonstrated in Figure 8, the OCA algorithm successfully detects the dense ice cloud at 06:00:00 UTC as a mixture of ice and multi-layered clouds. Interestingly, as time progresses, most of the formed line-shaped contrails are characterized as clouds by the OCA algorithm. We observe that many ice clouds are identified as clouds only in their central

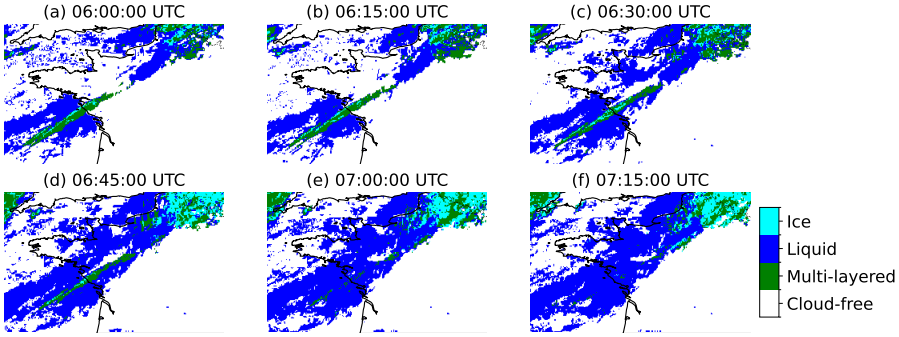

Figure 8. Cloud phase (cloud-free or multi-layered, liquid or ice cloud) as retrieved by the Optimal Cloud Analysis (OCA) algorithm for an example date and sequence of observation times (25th September 2023) in a zoomed geographic area where contrails are detected.

Table 3. Selected days, average number of ice and multi-layered cloud pixels, and average number of potential contrail pixels per observation, and percentage of ~~contrails~~ cirrus over the overall geographic region.

Day	Average number of ice and multi-layered cloud pixels	Average number of potential contrail pixels	Percentage of potential contrails
30-01-2023	122.146	30.880	25.28 %
13-06-2023	134.342	41.971	31.24 %
25-09-2023	129.806	43.196	33.28 %
30-01-2024	226.090	48.087	21.26 %
17-02-2024	258.712	59.403	22.96 %
28-05-2024	161.647	42.645	26.38 %

parts, while their thinner edges often remain undetected. We speculate that this is due to the spatial resolution of SEVIRI/MSG observations, which is 3x3 km^2 at the SSP.

As presented in Section 3.2, the application of a CTP filter distinguishes natural cirrus clouds from potential contrails. In the following section, we proceed with the generation of RF maps based on this distinction. Table 3 summarizes the average number of pixels characterized as ice and multi-layered clouds for each selected day per observation, as well as the percentage of these pixels having contrails. The day with the largest number of potential contrail pixels is the 17th of February 2024, followed by the 30th of January 2024.

4.2 Radiative forcing of contrails

~~Starting from this section and~~ From this section onward, the focus is exclusively on ~~contrail cirrus clouds.~~ potential contrail clouds: A net RF value was assigned to the pixels characterized as ice or multi-layered clouds that passed the distinguishing filter between ~~natural and contrail cirrus clouds~~low- and high-altitude ice clouds, the latter representing contrails in this work.

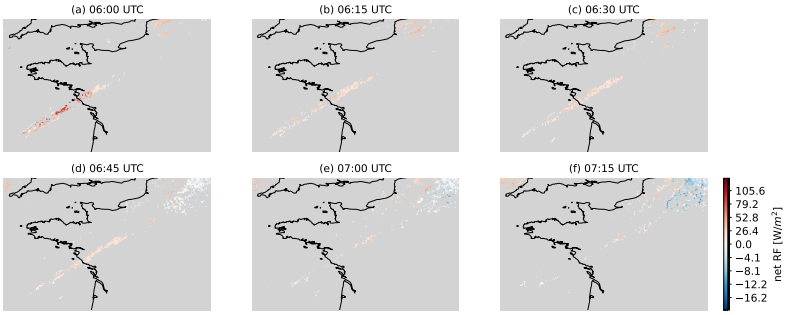

Figure 9. Net radiative forcing (RF) (sum of SW and LW RF) of contrails for an example date and sequence of observation times (25th September 2023) in a zoomed geographic area with detected ~~contrails~~contrail cirrus.

The net RF is calculated as the sum of RF_{sol} + RF_{tir}. As discussed in Section 2.3, the presence of an ice cloud ~~results~~ is most commonly expected to result in cooling in the SW wavelength region (negative RF values) and warming in the LW wavelength region (positive RF values).

Figure 9 ~~shows maps of contrail~~ presents maps of contrails net RF for the same geographic region as in Figures 7 and 8 on the 25th of September, 2023, from 06:00:00 UTC to 07:15:00 UTC. For this sequence of observation times, the detected contrails exhibit a positive radiative effect, indicating that the overall effect was warming during these early morning hours. At 06:00 UTC, the long, thin ice cloud mostly located above the Atlantic exhibits the strongest warming effect compared to other ice clouds during the rest of the time period, likely due to the still nighttime conditions in this region. As daytime progresses and the sun rises, the warming effect of the contrails diminishes, indicating that the shortwave cooling effect becomes more pronounced.

An overall daily view of the RF effect of contrails is provided in Figure 10. Over the geographic region of interest and for the six selected days, the net RF values of the detected ice or multi-layered cloud pixels have been multiplied by the coverage area per pixel, summed and then divided by the total coverage area for all the pixels. We refer to this summation as the total ~~RF_{all}~~RF_{ice}. Additionally, summing up only the ~~contrail~~ contrails pixels will provide us the total $RF_{contrail}$. For the example day of 25th of September 2023 (Fig. 10 (c)), the total net RF values of the contrails range from ~~-24.18~~ -3.71 W/m^2 (12:00 UTC) to ~~31.99~~ 3.90 W/m^2 (23:30 UTC). As it is expected, for all the selected days, the maximum total net $RF_{contrail}$ appears during nighttime due to the absence of SW cooling, while the minimum $RF_{contrail}$ value occurs during daytime and close to each midday. Even though the largest number of potential contrail pixels is found during the 17th of February 2024, we observe that the absolute maximum $RF_{contrail}$ values are observed during the 13th of June 2023 (see Table 3). This is due to the increased incoming solar radiation during the warmer months in the Northern Hemisphere compared to the colder months. Additionally, the contribution of the LW RF to the total RF for the detected ice and multi-layered clouds, and contrail pixels is

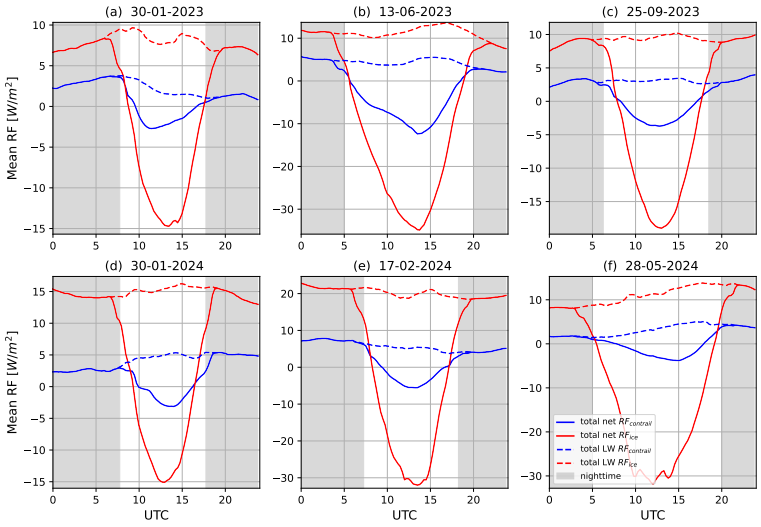

Figure 10. Time series of total net and longwave (LW) radiative forcing (RF) in W/m^2 for all the detected ice and multi-layered clouds (represented by solid and dashed red lines) and for only the ~~detected as~~ potential contrails (represented by solid and dashed blue line) above the overall geographic area for the six selected days. The shaded grey background indicates nighttime.

~~shown~~ presented in each subplot in Figure 10. It is observed that, for each case, the LW consistently contributes positively to the total RF throughout the day, with small fluctuations observed across different cases.

5 Validation of the Rapid Contrail-RF Estimation Approach

The accuracy and reliability of the Rapid Contrail-RF Estimation Approach in constructing RF maps for contrails have been investigated through ~~four~~ five different validation exercises, presented in the following subsections. These exercises focus on different aspects of the methodology. First, we evaluate the choice of using a single atmospheric vertical profile in the RT simulations (Subsection 5.1). Next, by performing a small subset of RT simulations, we investigate the impact of selecting a certain ice cloud parameterization scheme (Subsection 5.2). Additionally, we evaluate the impact of using CTH values estimated by a single atmospheric vertical profile on the RF estimations ~~. Finally~~(Subsection 5.3). Then, we perform a comparison between the flux maps for contrails and polar-orbiting satellite observations (Subsection 5.4). Finally, a comparison between our results and those reported in Wang et al. (2024) for two contrail cirrus outbreaks is also presented.

5.0.1 ~~Impact of vertical temperature profile on radiative transfer calculations~~

5.1 Impact of vertical temperature profile on radiative transfer calculations

The core component of the Rapid Contrail-RF Estimation Approach is the construction of the ice cloud RF LUTs and their merging with the re-gridded geostationary maps (see Section 3.1). As presented in Section 2.3, the atmospheric temperature vertical profile used in the RT simulations remains constant and corresponds to the U.S. Standard Atmosphere.

To assess the validity of this choice and estimate the uncertainty associated with using a single constant temperature vertical profile, randomly selected pixels from the zoomed geographic regions of each day-containing contrails above land, ocean, and liquid water clouds (i.e., multi-layered)-covering day- and night-time conditions were chosen as the sample of this investigation. For these selected pixels, RT simulations were performed using the ERA5 vertical temperature profile from ECMWF (see Section 2.4) as the input atmospheric profile. These profiles were also used to estimate CTH and wCTH (only in the presence of a liquid water cloud). Additionally, for each pixel, the actual CER and COT values from the OCA product were used, along with the real SZA. In the presence of a liquid water cloud, we use the wCOT value from the OCA product.

In Figure 11, for each scene scenario, we present the comparison results between the RF values coming from the LUTs ($RF_{USstandard}$) and the RF values calculated by using the actual atmospheric and cloud conditions (RF_{ERA5}) per selected pixel in the SW and LW wavelength ranges, separately. As it can be seen, for all the scene scenarios in the SW wavelength range, overall good agreement is found with the correlation coefficient ~~and slope values being close to unity~~(R) ranging from 0.97 to 1.00 and slope (s) from 0.93 to 0.97, with the exception of a few comparison points. Table 4 provides some statistics for the two different methodologies followed in this Section per wavelength and scene scenario. In the SW wavelength range, the use of LUTs instead of real-time RT simulations per pixel can lead to RMS error ~~equal to 6.13 W/m^2, 10.76 W/m^2, and 11.99 W/m^2~~ percentage equal to 6.30 %, 7.32 %, and 17.56 % above land, ocean, and liquid water cloud, respectively. The comparisons in the LW wavelength range (see Figure 11) reveal an overall good agreement with correlation coefficient values being around 1.00 and slope values in the range of 0.95 - 0.97. In contrast to the comparison in the SW, in the LW, we observe that a larger number of points appears to be scattered around the 1:1 line. This finding means that the RT simulations in the LW wavelength range are more sensitive in the choice of the atmospheric temperature vertical profile. The use of LUTs in the LW wavelength range leads to RMS error values of the same order of magnitude for the three scene scenarios. When focusing on the SW and LW RMS error percentage, we find that the largest values for both wavelength ranges are observed for the scene scenario of an ice cloud above a liquid water cloud (multi-layered).

To explain the scattered points around the 1:1 line in the subplots of Figure 11, we focus on the points with an RMS error value larger than the mean RMS error value plus two times the standard deviation of the RMS error. For these points, we first investigated whether there is a correlation between the large discrepancies in the two RF datasets and the differences between the values of each actual cloud parameter and the closest values used during the multi-dimensional interpolations in the LUTs. The comparison results ~~showed~~ depicted no correlation.

Additionally, for these points, we examine the corresponding ECMWF vertical profiles used in the RTM simulations. Figure 12 illustrates the temperature and humidity of the US Standard profile, along with the median profile of the ECMWF verti-

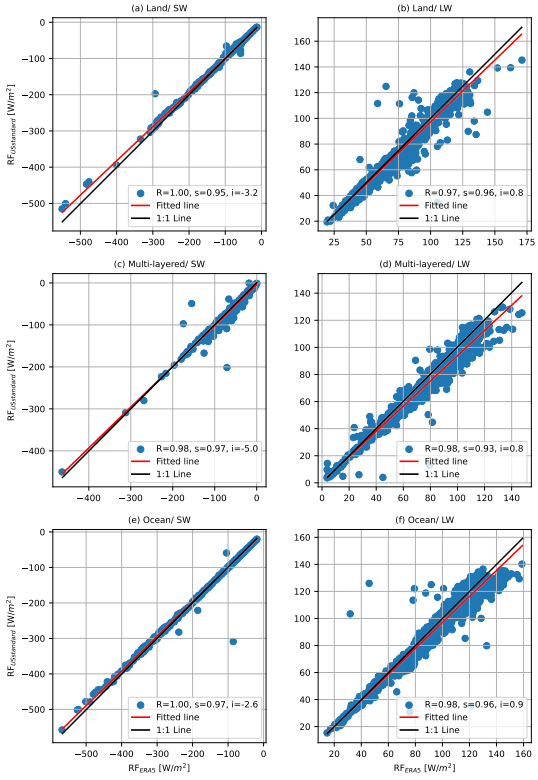

Figure 11. Scatter plot between radiative forcing (RF) values estimated by using the Look-Up Tables (LUTs) (RF_{LUTs}) and radiative transfer calculations using the actual atmospheric temperature vertical profiles (RF_{actual}) for randomly selected pixels containing potential contrails above land surfaces in the (a) SW, and (b) LW, underlying liquid water clouds (i.e., multi-layered) in the (c) SW and (d) LW, and ocean surfaces in the (e) SW and (f) LW.

cal profiles, as well as the coverage of these profiles. We observe that the coverage of the ECMWF vertical profiles ~~shows~~ demonstrates different values for surface temperatures but their median profile agrees very well with the US Standard atmospheric profile. In contrast, the humidity ECMWF vertical profiles ~~show~~ depict a large difference at the surface compared to the US Standard profile.

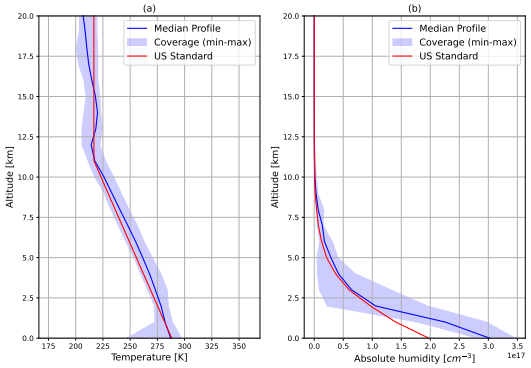

Figure 12. Vertical (a) temperature and (b) humidity profiles of US Standard atmosphere, median profiles of the ECMWF vertical profiles corresponding to the largest discrepancies (i.e., large RMS error percentage between radiative forcing (RF) values estimated by using the Look-Up Tables (LUTs) (RF_{LUTs}) and radiative transfer calculations using the actual atmospheric temperature vertical profiles) for the six selected days.

Table 4. Mean radiative forcing (RF) values over all the randomly selected pixels for the six selected days, bias, RMS error, RMS error percentage, and mean percent errors between RF values estimated by using the Look-Up Tables (LUTs) and by using the ERA5 atmospheric profile and the OCA cloud conditions for the SW, and LW estimated RFs.

	Mean RF value (USstandard) (W/m^2)	**Mean RF value (ERA5)** (W/m^2)	**Bias** (W/m^2)	**RMS Error** (W/m^2)	**RMS Error percentage (%)**	**Mean bias percentage (%)**
Land/ SW	-95.28	-97.27	1.99	6.13	6.30	2.05
Multi-layered/ SW	-71.21	-68.28	-2.93	11.99	17.56	4.29
Ocean/ SW	-145.49	-146.97	1.48	10.76	7.32	1.01
Land/ LW	84.46	86.74	-2.29	7.53	8.68	2.64
Multi-layered LW	61.35	65.23	-3.88	7.01	10.75	5.95
Ocean/ LW	95.32	98.19	-2.88	7.24	7.37	2.93

460 Overall, in the SW wavelength range, the use of a standard profile in the construction of the LUTs lead to mean bias percentage of about 2.05%, 1.01%, and 4.29% for a contrail above land, ocean, and liquid water cloud, respectively. In the LW

wavelength range, the mean percent errors equal to 2.64%, 2.93%, and 5.95% for a contrail above land, ocean, and liquid water cloud, respectively.

5.1.1 ~~Impact of ice cloud parameterization on radiative transfer calculations~~

5.2 Impact of ice cloud parameterization on radiative transfer calculations

The micro-physical properties of the ice crystals, which are part of the ~~cirrus cloudsand contrails~~ice clouds, play a crucial role in their single scattering properties and, consequently, the RF of these clouds (Stephens et al., 1990; Sanz-Morère et al., 2020). Here, we assess the impact related to the choice of ice cloud parameterization in the RT simulations. The parameterization determines how the ice water content and CER are translated into optical properties. Since the ice crystal shape is an unknown parameter, we have selected the parameterization by Yang et al. (2013), assuming the ice crystal habit to be a column composed of 8 elements with a moderate degree of roughness, as this is the habit most frequently observed for thin ice clouds (Forster and Mayer, 2022) and contrails (Järvinen et al., 2018). According to the same study, 60 % of cirrus clouds are a mixture of ice crystals with severe roughness, while 40 % a mixture of smoothed ones. Similarly to Wolf et al. (2023), we have chosen a moderate degree of roughness for the simulations included in the LUTs.

For this sensitivity study, we performed a small subset of RT simulations in the SW and LW wavelength ranges, varying the choice of ice cloud parameterization. We selected all the available ice crystal shapes from the parameterization by Yang et al. (2013). In addition, we included the parameterization by ~~Fu (1996); Fu et al. (1998)~~Fu (1996), and by Fu et al. (1998), which is operationally applied in the ECMWF Integrated Forecasting System (IFS) and assumes ice crystals as pristine hexagonal columns. The simulations are always performed for an ice cloud with a COT equal to 0.5 to maximize its semi-transparency and, subsequently, the effect of cloud microphysics. We have chosen three different SZA values (10^o, 40^o, and 70^o), a CER of 20 μm, and a CTH of 10 km. For these simulations, the ice cloud is located above an ocean surface characterized by three different SST values (273 K, 293 K, and 303 K).

Figure 13 ~~shows~~ presents RF_{sol} as a function of various ice crystal habits based on the parameterization of Yang et al. (2013) (i.e., column with 8 elements, droxtal, hollow bullet rosette, hollow column, plate, plate with 10 elements, plate with 5 elements, solid bullet rosette, and solid column) and their degrees of roughness (smooth, moderate, and severe) for three different SZAs. The ice crystal habit of an hexagonal column by Fu (1996) is included as well. Additionally, the figure presents the relative differences in RF_{sol} compared to the selected ice crystal shape and degree of roughness for the construction of the LUTs. As observed, the choice of ice crystal habit and roughness degree can result in large differences, which can be up to 60% (e.g., the case for SZA = 10^o for smooth plates of 10 elements) in the SW wavelength range. In addition, the parameterization of Fu (1996), which assumes a pristine hexagonal column results in differences up to approximately 20 % for the case of a small SZA. For the three SZA scenarios, RF_{sol} of the selected ice crystal shape and roughness appears to have the lowest values compared to other ice crystal shapes and degrees of roughness.

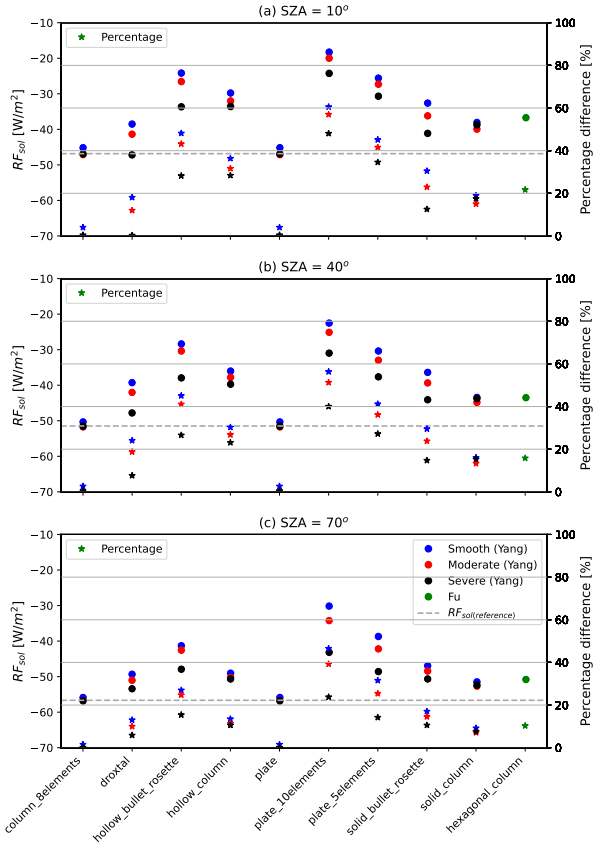

Figure 13. Simulated radiative forcing values in the shortwave (i.e., solar) wavelength range (RF_{sol}) are ~~shown~~ presented as a function of various ice crystal habits and their degrees of roughness (shown with circles) based on the parameterization of Yang et al. (2013) and Fu et al. (1998) for three different solar zenith angle (SZA) scenarios. The horizontal line (i.e., grey dashed line) represents the $RF_{sol(reference)}$ value for the selected ice crystal shape and roughness used in this study. The percentage difference between each ice crystal habit and the one used in the LUTs is denoted by star symbols.

Figure 14 ~~shows~~ presents RF_{tir} as a function of the same ice crystal habits and roughness degrees for three different SST scenarios, along with their relative differences. In contrast to the shortwave range, the differences in the LW (RF_{tir}) are much smaller, not exceeding 12%.

From the sensitivity tests, we conclude that ice crystal habit and roughness can lead to significant differences in RT simulations in the SW wavelength region, while these factors play a less significant role in the LW wavelength region. When investigating the simulated upward and downward irradiance at TOA in the SW wavelength region, we find that the largest differences between the selected ice crystal shape and roughness (i.e., column of 8 elements with moderate roughness) and a

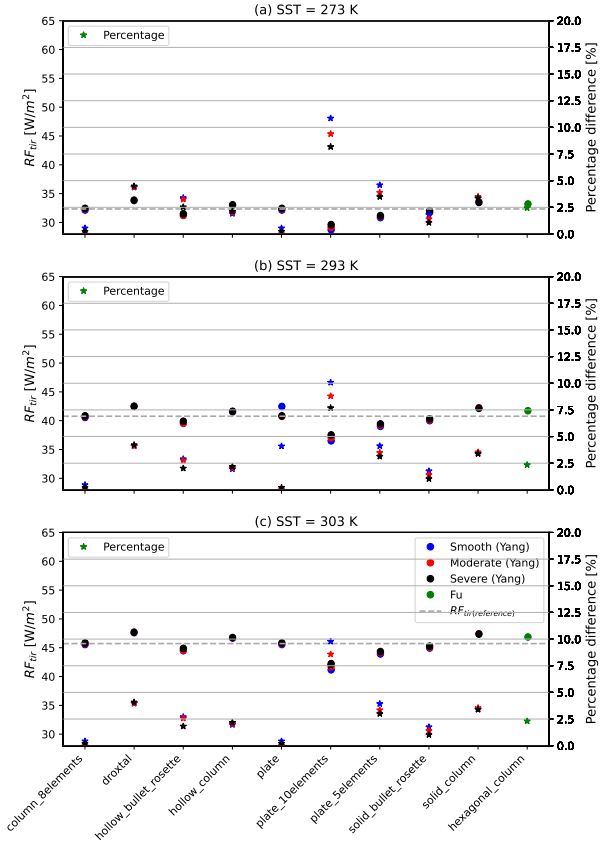

Figure 14. Similar as Figure 13 but for the longwave (i.e., thermal infrared) wavelength range, where RF_{tir} values are ~~shown~~ presented for three different sea surface temperature (SST) scenarios.

plate of 10 elements with a smooth degree of roughness (i.e., largest differences in RF_{sol}) occur in the following wavelength ranges: 1122 - 1135 nm, 1346 - 1471 nm, 1800 - 1954 nm, and 2486 - 2752 nm. Similarly, in the LW wavelength, the simulated spectrum is affected the most by the choice of the ice crystal shape and roughness in the following wavelength ranges: 3487 - 4171 nm, 4645 - 5502 nm, and 8113 - 9153 nm.

To estimate the uncertainty associated with the selection of a specific ice cloud parameterization in the RF_{sol} and RF_{tir} maps, we have re-performed the RT simulations for the randomly selected pixels (see Section 5.1 for only a single day; 25-09-2023). Consequently, the comparison is made between RF_{sol} and RF_{tir} obtained in Section 5.1, where the default ice cloud parameterization was applied, and those generated by employing the same input values for the RT simulations, but differing the choice of ice cloud parameterization. For the comparison, we have used the ice crystal habit and roughness, which exhibits the largest difference with our default settings: plate of 10 elements with a smooth degree of roughness (Yang et al., 2013).

Table 5 summarizes the findings of the above-mentioned comparison. As expected by the sensitivity study, the use of another ice crystal habit and roughness can lead to large differences in the SW and slightly affects the LW wavelength range. For the SW wavelength range and for all the scene scenarios, the mean RF values for columnar and plate ice crystals differ by a negative bias, with the largest bias found for contrails above ocean surfaces (-49.33 W/m^2).

For the LW wavelength range, the bias values are smaller, with the largest bias being equal to 5.89 W/m^2 for ice clouds above liquid water clouds (i.e., multi-layered).

We should keep in mind that actual measurements of the micro-physical properties of ice crystals in contrail clouds are rare and difficult to obtain. There have been in-situ measurements, such as those in Järvinen et al. (2018), which found that the primary ice crystal habit is aggregates (i.e., the one used in this study), though the presence of other crystal shapes has been reported. Consequently, we used the most common one to optimize the representation of ice crystals. However, applying a single ice crystal shape and roughness for the overall number of detected contrails during different seasons, and above various scenes may not be fully representative.

Table 5. Mean radiative forcing (RF) values over all the randomly selected pixels for the 25th of September 2023, bias, RMS error between RF values when using an ice crystal habit of column with 8 elements and a plate with 10 elements for the SW, LW, and net estimated RFs.

	Mean RF value (column 8elements) (W/m^2)	**Mean RF value (plate 10elements)** (W/m^2)	**Bias** (W/m^2)	**RMS Error** (W/m^2)
Land/ SW	-77.14	-42.70	-34.44	37.36
Multi-layered/ SW	-66.65	-34.39	-32.26	41.57
Ocean/ SW	-133.52	-84.19	-49.33	60.08
Land/ LW	63.20	58.37	4.83	5.24
Multi-layered LW	47.08	41.19	5.89	7.13
Ocean/ LW	65.55	67.29	-1.75	15.26

5.2.1 ~~Impact of Cloud Top Height (CTH) on radiative forcing interpolation~~

5.3 Impact of Cloud Top Height (CTH) on radiative forcing interpolation

As mentioned in Section 2.2, the OCA product provides the CTP. To have the information about CTH, which is used as a parameter in the RT calculations in the LW wavelength range, the US Standard profile is used. More precisely, we linearly interpolate the CTP in the pressure vertical grid, and consequently, the altitude vertical grid, of the US Standard atmospheric profile.

CTH plays an important role in the LW wavelength range, where it is utilized to perform the multi-dimensional interpolation of the simulated RF_{tir} values from the LUT at the actual values of the cloud and environmental parameters for each pixel.

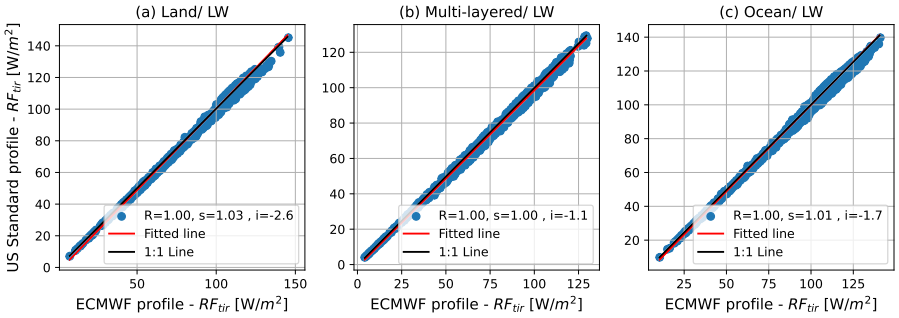

Figure 15. Scatter plots between radiative forcing (RF) values estimated by using the cloud top height (CTH) as estimated by the US Standard profile and by the ECMWF temperature profiles for randomly selected pixels containing ~~a contrail~~ potential contrails above (a) land surfaces, (b) underlying liquid water clouds and (c) ocean surfaces in the LW wavelength range.

To evaluate the accuracy of using a constant atmospheric profile to estimate the CTH, we have selected the same pixels as in Section 5.1. For these pixels, ECMWF pressure vertical profiles were used to interpolate linearly the contrail CTP in the altitude vertical grid of those profiles. Consequently, this CTH value, named 'CTH - ECMWF', in every selected pixel can be used to re-perform the multi-dimensional interpolation in the parameters and estimate a new RF value in the LW wavelength range.

Figure 15 ~~shows~~ presents the comparisons between this new RF value by using the actual CTH and a CTH estimated by the US Standard profile. As we can see, the correlation between them is excellent for the three different scene scenarios, indicating that using a different CTH value does not affect the multi-dimensional interpolation performed in the LUTs to extract the RF_{tir}. As it is ~~shown~~ demonstrated in Figure 16, for the three different scene scenarios, the CTH values estimated by using a real atmospheric and the US Standard profile ~~show~~ depict small differences with a mean bias equal to 0.85 %, -0.60 %, and -1.70 % above land, ocean, and liquid water cloud, respectively. The scatter plots of Figure 16 reveal that for the three scene scenarios, CTH estimated by the US Standard profile is systematically lower by 22 - 26 % compared to the CTH estimated by the ECMWF vertical profiles.

5.4 Comparison of estimated flux maps and CERES observations

TOA upward solar (i.e., SW) and thermal infrared (i.e., LW) fluxes, as observed by the CERES FM1 and FM3 instruments, have been used to validate the first output after merging the datasets in the Rapid Contrail-RF Estimation Approach: the TOA upward SW and LW fluxes referred to as F_{up} (see Equation 1). This comparison focuses exclusively on pixels identified as potential contrail pixels.

The comparison was conducted using data from the six selected days. For each of these days, the closest-in-time MSG/-SEVIRI observation was matched with the CERES observations (approximately four per day above the zoomed geographic region of interest) by taking into account the exact acquisition time of the selected MSG/SEVIRI pixels. Since CERES has a larger footprint (approximately 25 km in diameter near nadir) compared to the spatial resolution of the flux maps generated by

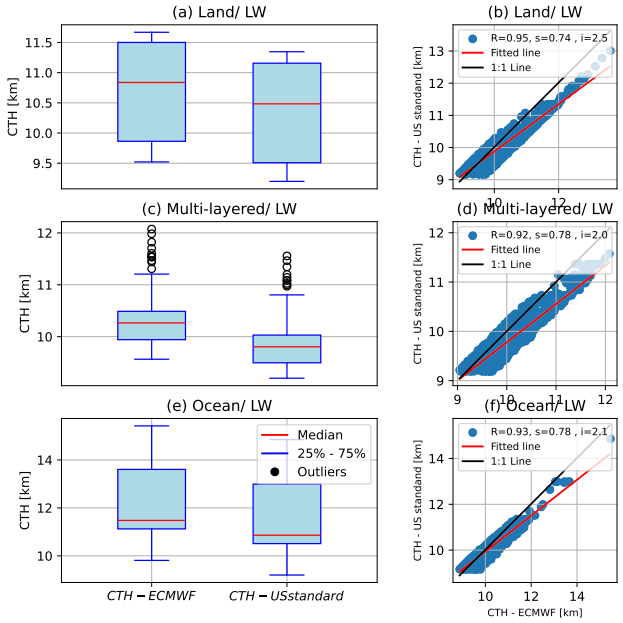

Figure 16. Box-Whisker plots of cloud top height (CTH) values as estimated by the US Standard profile and by actual temperature profiles from ECMWF for randomly selected pixels containing ~~a contrail~~ potential contrails above (a) land surfaces, (b) underlying liquid water clouds and (c) ocean surfaces in the LW wavelength range.

the Rapid Contrail-RF Estimation Approach, we averaged the ~~contrail cirrus~~ potential contrail pixels, which are located inside the CERES footprint. To perform this averaging, we defined ~~a circular area with a radius of 12.5 km~~ an ellipsoid area around the latitude and longitude of CERES field-of-view (FOV) at surface, based on the satellite's height, viewing zenith angle, and the clock angle of CERES FOV at satellite. If this area was ~~fully covered of contrail pixels~~covered of potential contrail pixels more than 75%, we averaged these pixels and compared them with the CERES fluxes in the SW and LW wavelength ranges, separately.

Figure 17 ~~shows~~ presents the outcome of the comparison described above. As seen, there is generally good agreement in the SW and LW wavelength range, with a correlation coefficient (R) of ~~0.90 and 0.85~~0.99 and 0.86, respectively.

Table 6 provides ~~some~~ overall statistics for the mean CERES and Rapid Contrail-RF Estimation-estimated upwards TOA fluxes. The bias in the SW wavelength range (~~6.92~~ 1.28 W/m^2) indicates that the Rapid Contrail-RF Estimation Approach, in general, slightly overestimates the SW fluxes by ~~2.33~~1.05% compared to CERES, while in the LW wavelength range the bias is negative (~~-12.20~~ -16.24 W/m^2) indicating that our approach underestimates in general the LW fluxes by ~~7.67~~ 9.07 % compared to CERES. Additionally, the higher Rapid Contrail-RF Estimation Approach SW fluxes compared to CERES align with the RF_{sol} values for the ice cloud microphysics in Section 5.2. There, it was ~~shown~~ demonstrated that using column of 8 elements as the ice crystal shape results in the lowest radiative forcing values compared to other ice crystal shapes. Concerning the RMS error, the Rapid Contrail-RF Estimation Approach seems to perform better in estimating LW fluxes than SW ones.

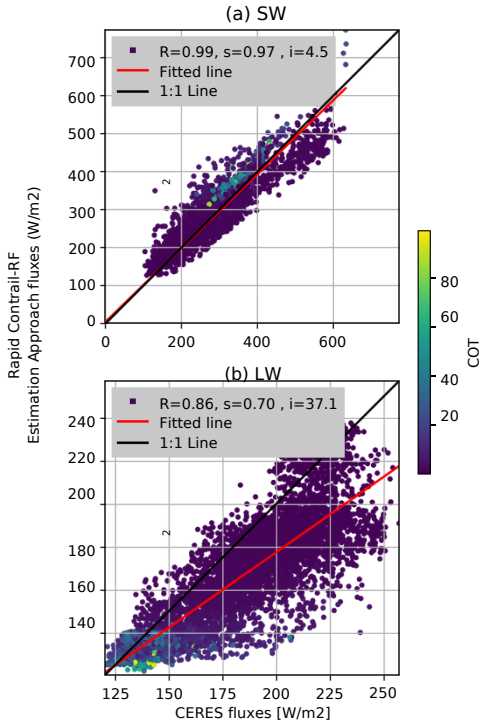

Figure 17. Scatter plots of TOA fluxes observed by CERES and estimated by using the LUTs in the shortwave (SW, upper plot) and longwave (LW, lower plot) wavelength ranges. The points of each plot are color-coded based on the mean ~~contrail~~ contrails optical thickness (COT for cloud optical thickness), averaged within the respective CERES footprints.

However, we observe that in LW wavelength range, the two compared fluxes exhibit the largest scattering, resulting in many points having considerably lower fluxes compared to CERES ones.

Focusing on the mean ~~contrail~~ cirrus optical thickness (COT) values, averaged within the respective CERES footprints and color-coded in Figure 17, we observe that in the LW wavelength region, the largest COT values correspond to cases in which the Rapid Contrail-RF Estimation Approach retrieves low fluxes (smaller than 140 W/m^2), while the CERES fluxes ~~show~~ demonstrate larger variability. In the SW wavelength, there is no direct correlation between mean contrail optical thickness values and discrepancies between the two datasets.

Table 6. Mean CERES and Rapid Contrail-RF Estimation Approach-estimated upwards TOA fluxes, bias and RMS error for the SW and LW wavelength range.

Wavelength range	Mean CERES fluxes (W/m^2)	Mean Rapid Contrail-RF Estimation fluxes (W/m^2)	Bias (W/m^2)	RMS Error (W/m^2)
SW	~~296.60~~ 121.58	~~303.52~~ 122.85	~~6.92~~ 1.28	~~44.12~~ 27.21
LW	~~159.03~~ 178.98	~~146.82~~ 162.75	~~-12.20~~ -16.24	~~18.33~~ 23.11

5.5 Comparison with an existing study

A direct comparison has been conducted between the outputs of the Rapid Contrail-RF Estimation Approach and the results reported in Wang et al. (2024). In that study, the authors investigated the radiative effects of two contrail cirrus outbreaks over Western Europe using geostationary satellite observations and radiative transfer calculations. Our primary motivation for this specific comparison is the use of a common geostationary satellite and cloud product (a modified OCA product; see below).

The two outbreaks extended over Western Europe on two consecutive days, 22 and 23 June 2020. For these days, Dust/RGB images from the MSG/SEVIRI satellite were used to visually demonstrate the two outbreaks. We now describe the methods used by the authors of Wang et al. (2024): Radiative transfer simulations were then conducted using ecRad as the radiative transfer code. The required input for ice cloud properties was derived from the OCA product, modified by increasing the COT values by a multiplicative factor of 1.3. The ice crystals were assumed to be pristine hexagonal columns. Atmospheric vertical profiles were obtained from the ECMWF Reanalysis version 5 (ERA5). Consequently, both studies share common components in their methodology but also exhibit important differences.

Figure 18 shows the net RF values of the contrails during the first outbreak from 09:00 UTC to 22:00 UTC on 22 June 2020, focusing on the same geographic region as in Wang et al. (2024). This figure corresponds to Figure 2 in Wang et al. (2024). A first qualitative comparison between the two figures clearly reveals the warming effect of contrails over land. However, in our case, at 12 UTC, we observe mainly cooling over ocean, whereas in Wang et al. (2024), the ice clouds exhibit both cooling and warming effects. At 18 UTC, the pattern is reversed.

We conducted a quantitative comparison to assess the net total power of the SW, LW, and net RF of ice clouds and clouds with CTP above 300 hPa, expressed in terrawatt (TW), over the region of interest from 07:00 UTC on 22 June 2020 to 12:00 UTC on 23 June 2020. We used the online tool WebPlotDigitizer (https://automeris.io/) to extract the SW, LW, and net total radiative effect of the both the ice clouds and those located above 300 hPa from Figures 3b, S6a, and S6b in Wang et al. (2024) , which we could then compare directly to our own values. As shown in the comparisons in Figure 19, both datasets,total ice clouds and above 300 hPa, exhibit excellent agreement in terms of correlation coefficient values for SW, LW and net total

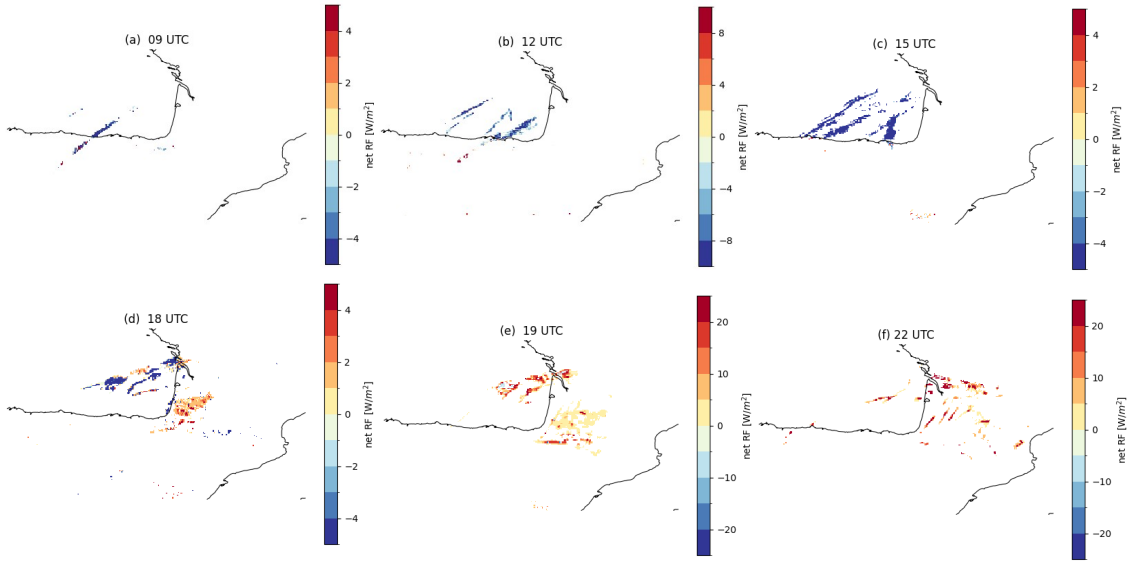

Figure 18. Maps of the net radiative forcing (RF) of ice clouds over the study region presented in (Wang et al., 2024), shown at six different times on 22 June 2020.

power over the geographic area of interest. However, the Rapid-Contrail Estimation Approach systematically yields smaller values compared to the results of Wang et al. (2024) as reflected in the slope values in Figure 19.

6 Conclusions

Quantifying the radiative forcing of ~~aviation-induced clouds and~~ contrails remains an active area of research, primarily due to significant uncertainties surrounding their overall contribution to climate change. In this study, a new satellite-based ~~contrail~~ contrails radiative forcing mapping is presented and evaluated. The so-called Rapid Contrail-RF Estimation Approach combines geostationary satellite observations, a cloud properties retrieval algorithm, radiative transfer modeling and a simplistic separation scheme between natural and ~~contrail cirrus~~ contrails clouds.

For six selected days within the 2023-2024 period, during which potential contrails were visually identified, MSG/SEVIRI data in combination with the OCA product were used for the detection and characterization of contrail ~~cirrus~~ clouds and aviation-induced cloudiness. The central focus of this study is the application of pre-computed RF LUTs for thin to semi-transparent ice clouds in both SW and LW spectral regions. SW and LW RF values were assigned to pixels identified as ice clouds using a multi-dimensional interpolation scheme. This methodology is computationally fast, avoiding the need for real-time radiative transfer simulations, and enabling the processing of large datasets.

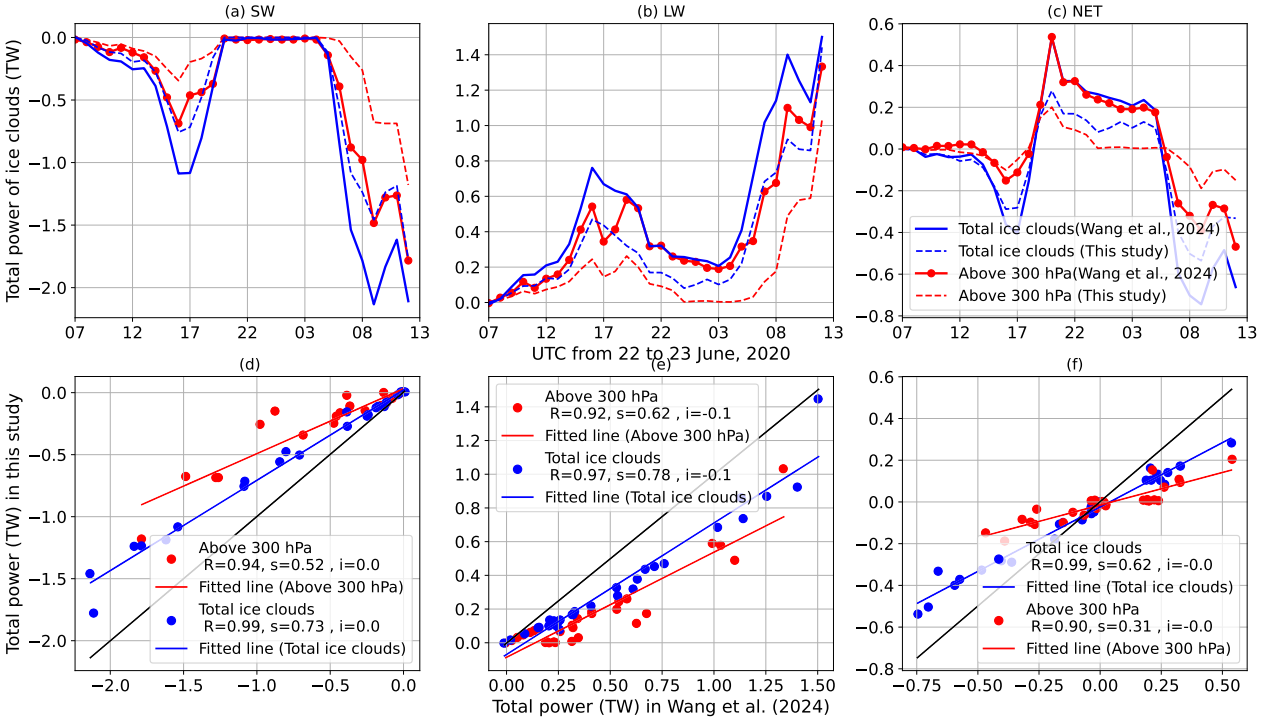

Figure 19. Time series of SW (panel a), LW (panel b), and net (panel c) total power of the ice cloud radiative effect over the study region from 07:00 UTC on 22 June 2020 to 12:00 UTC on 23 June 2020, for both the total ice cloud amount (blue lines) and ice clouds located above 300 hPa (red lines) in the two studies. Panels (d-f) show scatter plots comparing the total power values reported in (Wang et al., 2024) and those obtained in this study for the SW (d), LW (e), and net (f) wavelength ranges.

The primary aim of this study was to evaluate the validity and limitations of using RF LUTs in this context. This evaluation was conducted through ~~four~~ five different validation exercises. The first three focused on (1) the choice of using a single atmospheric vertical profile for the LUTs construction, (2) the choice of using one single ice cloud parameterization scheme and finally, and (3) the impact of using CTH values estimated with a standard profile during the merging of the cloud product with the LUTs. The fourth validation exercise is an end-to-end validation, comparing contrail flux maps generated by the Rapid Contrail-RF Estimation Approach with those derived from CERES instruments. Finally, the fifth validation is a comparison between our results and those reported in Wang et al. (2024) for two contrail cirrus outbreaks is also presented.

The main findings of the first three validation exercises are as follows:

1. Using a single standard atmospheric profile - in this study, the US Standard atmospheric profile - for constructing RF LUTs generally provides promising results over the region of interest. Indeed, this assumption can introduce biases of

up to -2.93 W/m^2 and -3.88 W/m^2 in the SW and LW wavelength range, respectively, which are considerably smaller compared to the respective fluxes.

2. Using a single ice crystal habit - in this study, a column composed of 8 elements with a moderate degree of roughness - for constructing the RF LUTs can lead to significant differences in the SW wavelength region. In the LW wavelength region, RF values are less sensitive to this selection. Using the most extreme difference scenario, which does not necessarily reflect reality, the choice of ice crystal habit can result to biases of up to -49.33 W/m^2 and 5.89 W/m^2 in the SW and LW wavelength range, respectively.

3. Using a CTH estimated from a single standard atmospheric profile during the merging of the cloud product with the RF LUTs leads to small differences in the LW wavelength range (i.e., biases of up to -1.70 W/m^2).

The end-to-end validation, which compared contrail cirrus flux maps generated by the Rapid Contrail-RF Estimation Approach with those derived from CERES instruments, yielded encouraging results concerning the performance of the Rapid Contrail-RF Estimation Approach. The mean biases are found to be ~~6.92~~ 1.28 W/m^2 and ~~-12.20~~ -16.24 W/m^2 for the SW and LW wavelength ranges, respectively. The observed biases can be partially attributed to the selected ice crystal habit, as the chosen habit tends to produce the lowest RF values compared to the other options.

Averaging all the mean biases percentage from the different correlative comparison in the LW and SW wavelength ranges, we find that our approach provides accurate data for estimating ~~contrail~~ contrails radiative forcing, with an accuracy on the order of approximately 15 %.

The resulting contrail RF maps revealed that, for the six selected days in this study, the presence of contrails causes warming during nighttime and cooling during daytime. The total daily mean net RF values caused by contrails over the entire geographic area of this study were calculated as follows: ~~6.91~~ 0.68 W/m^2 (25-09-2023), ~~3.05~~ 0.25 W/m^2 (28-05-2024), ~~11.11~~ 1.86 W/m^2 (30-01-2023), ~~-12.09~~ -2.31 W/m^2 (13-06-2023), ~~8.23~~ 1.86 W/m^2 (30-01-2024), and ~~9.93~~ 2.46 W/m^2 (17-02-2024). During the only summer month included in the analysis, the total daily mean net RF value is negative indicating that the SW contribution to the net RF in larger than the LW contribution. This is due to the increased incoming solar radiation during the warmer months in the Northern Hemisphere compared to the colder months. The total daily mean net RF values caused by contrails over the entire geographic area of this study were calculated as follows: 0.68 W/m^2 (25-09-2023), 0.25 W/m^2 (28-05-2024), 1.86 W/m^2 (30-01-2023), -2.31 W/m^2 (13-06-2023), 1.86 W/m^2 (30-01-2024), and 2.46 W/m^2 (17-02-2024). During the only summer month included in the analysis, the total daily mean net RF value is negative indicating that the SW contribution to the net RF in larger than the LW contribution. This is due to the increased incoming solar radiation during the warmer months in the Northern Hemisphere compared to the colder months.

To conclude, our study presents a new satellite-based contrail radiative forcing mapping. Performing various validation exercises, we demonstrate that this method provides reliable SW, LW and net RF maps for ~~contrail cirrus~~ potential contrail clouds. Based on these findings, future steps could include extending this study to cover a full year, which we believe will offer valuable insights into the seasonal behavior of contrails. Furthermore, leveraging more advanced geostationary satellites with higher spatial and temporal resolution, such as Meteosat Third Generation/ Flexible Combined Instrument (MTG/FCI)

would contribute in a better detection and monitoring of contrails. Finally, implementing an improved separation scheme between contrails and ~~natural cirrus clouds - such as a contrail detection algorithm~~ naturally occurring ice clouds –such as contrail detection algorithms based on neural networks ~~as proposed by Ortiz et al. (2025) - would enhance the detection of contrails~~(Ortiz et al., 2025)– is a necessary further step to perform radiation forcing studies for aviation-induced cloudiness.

Code and data availability. We have published the code to prepare an IGBP map and an example usage of the Look-UP Tables. Additionally, we provide the IGBP map on the reference domain, the NetCDF file for the look-up tables, and the timing of the SEVIRI images. This material has been published on Zenodo: https://zenodo.org/records/14859250

Author contributions. ED designed the validation of the Rapid Contrail-RF Estimation Approach, conducted the experiments, collected various datasets, performed the RT simulations, merged the principal datasets, carried out the data analysis, and wrote this paper. PdB contributed to preparing the land use dataset, providing the CERES observations, and developing the merging process of the principal datasets to generate the RF maps. NC conceived the initial idea for the validation of the Rapid Contrail-RF Estimation Approach and initiated the design of the LUTs. All authors contributed to and reviewed the final paper.

Competing interests. The contact author has declared that none of the authors has any competing interests.

Acknowledgements. This research work is part of the E-CONTRAIL project (https://www.econtrail.com/), funded from the SESAR Joint Undertaking (JU) under grant agreement No. 101114795. The authors gratefully acknowledge the E-CONTRAIL partners and the SESAR Joint Undertaking for their support, fruitful discussions during project meeting, and funding the E-CONTRAIL project. We would like to thank all the people who have contributed to the development of libRadtran software. Additionally, we would like to thank the Atmospheric Science Data Center at NASA Langley Research Center for providing the CERES data, as well as EUMETSAT for providing the MSG/SEVIRI and OCA data. Finally, we would like to thank Dr. Christine Aebi for proofreading this manuscript.

References

Anderson, G. P., Clough, S. A., Kneizys, F., Chetwynd, J. H., and Shettle, E. P.: AFGL atmospheric constituent profiles (0.120 0–120 km), UnknownTechnical Report AFGL-TR-86-0110, Air Force Geophysics Laboratory, Hanscom Air Force Base, Bedford, Mass., 1986.

Barkstrom

Barkstrom, B.: R.: CERES: The start of the next generation of radiation measurements, Advances in Space ResearchStart of the Next Generation of Radiation Measurements, Adv. Space Res., 24, 907–914, https://doi.org/10.1016/S0273-1177(99)00354-3, 1999.

Bier, A. and Burkhardt, U.: Impact of parametrizing microphysical processes in the jet and vortex phase on contrail cirrus properties and radiative forcing, Journal of Geophysical Research: AtmospheresJ. Geophys. Res. Atmos., 127, e2022JD036 677, https://doi.org/10.1029/2022JD036677, 2022.

Bock, L. and Burkhardt, U.: Reassessing properties and radiative forcing of contrail cirrus using a climate model, Journal of Geophysical Research: AtmospheresJ. Geophys. Res. Atmos., 121, 9717–9736, https://doi.org/10.1002/2016JD025112, 2016.

Brasseur, G. P., Gupta, M., Anderson, B. E., Balasubramanian, S., Barrett, S., Duda, D., Fleming, G., Forster, P. M., Fuglestvedt, J., Gettelman, A., et al.: Impact of aviation on climate: FAA's aviation climate change research initiative (ACCRI) phase II, Bulletin of the American Meteorological SocietyB. Am. Meteorol. Soc., 97, 561–583, https://doi.org/10.1175/BAMS-D-13-00089.1, 2016.

Burkhardt, U. and Kärcher, B.: Global radiative forcing from contrail cirrus, Nature climate changeNat. Clim. Change, 1, 54–58, https://doi.org/10.1038/nclimate1068, 2011.

Chen, C.-C. and Gettelman, A.: Simulated radiative forcing from contrails and contrail cirrus, Atmospheric Chemistry and PhysicsAtmos. Chem. Phys., 13, 12 525–12 536, https://doi.org/10.5194/acp-13-12525-2013, 2013.

Chen, T., Rossow, W. B., and Zhang, Y.: Radiative effects of cloud-type variations, Journal of climateJ. Climate, 13, 264–286, https://doi.org/10.1175/1520-0442(2000)013<0264:REOCTV>2.0.CO;2, 2000.

Cox, C. and Munk, W.: Measurement of the roughness of the sea surface from photographs of the sun's glitter, JosaJ. Opt. Soc. Am, 44, 838–850, 1954a.

Cox, C. and Munk, W.: Statistics of the sea surface derived from sun glitter, J. Marine Res., 13, 198–227, 1954b.

DEKOUTSIDIS

Dekoutsidis, G.and FEIDAS, H.: CONTRAILS AND CONTRAIL-CIRRUS CLOUDS CHARACTERISTICS BASED ON SATELLITE IMAGES AND THEIR RELATION TO THE ATMOSPHERIC CONDITIONS, Le Changement Climatique, la variabilitéet les risques climatiques, p. 391: Contrails and contrail-cirrus clouds characteristics based on satellite images and their relation to the atmospheric conditions, Presented at the XXXIIème Colloque International de l'AIC: Climatic Change, Variability and Climatic Risks, https://doi.org/10.13140/RG.2.2.12901.42728, 2019.

Dekoutsidis, G., Feidas, H., and Bugliaro, L.: Contrail detection on SEVIRI images and 1-year study of their physical properties and the atmospheric conditions favoring their formation over Europe, Theoretical and Applied ClimatologyTheor. Appl. Climatol., 151, 1931–1948, https://doi.org/10.1007/s00704-023-04357-9, 2023.

Driver, O. G., Stettler, M. E., and Gryspeerdt, E.: Factors limiting contrail detection in satellite imagery, Atmos. Meas. Tech., 18, 1115–1134, https://doi.org/10.5194/amt-18-1115-2025, 2025.

Duda, D. P., Minnis, P., Nguyen, L., and Palikonda, R.: A case study of the development of contrail clusters over the Great Lakes, Journal of the atmospheric sciences, 61, 1132–1146J. Atmos. Sci., 61, 1132–1146, https://doi.org/10.1175/1520-0469(2004)061<1132:ACSOTD>2.0.CO;2, 2004.

Duda, D. P., Bedka, S. T., Minnis, P., Spangenberg, D., Khlopenkov, K., Chee, T. , and Smith Jr, W. L.: Northern Hemisphere contrail properties derived from Terra and Aqua MODIS data for 2006 and 2012, Atmospheric Chemistry and Physics, 19, 5313–5330, 2019.

Emde, C., Buras-Schnell, R., Kylling, A., Mayer, B., Gasteiger, J., Hamann, U., Kylling, J., Richter, B., Pause, C., Dowling, T., et al.: The libRadtran software package for radiative transfer calculations (version 2.0. 1), Geoscientific ModelDevelopmentGeosci. Model. Dev., 9, 1647–1672, https://doi.org/10.5194/gmd-9-1647-2016, 2016.

EUMETSAT: MTG-FCI: ATBD for Optimal Cloud Analysis Product, doc.No.: EUM/MTG/DOC/11/0654. Available online at: https://user.eumetsat.int/s3/eup-strapi-media/pdf_mtg_atbd_oca_b1ba8fc34c.pdf, last access: 2024-10-17, 2016.

EUMETSAT: Local GRIB tables used at EUMETSAT, doc.No.: EUM/TSS/TEN/13/711807. Available online at: https://user.eumetsat.int/s3/eup-strapi-media/pdf_mpef_local_grib_descript_4b2b880d62.pdf, last access: 2024-09-24, 2019a.

EUMETSAT: Optimal Cloud Analysis Climate Data Record Release 1 - MSG - 0 degree, doc.No.: 10.15770/EUM_SEC_CLM_0049. Available online at: https://user.eumetsat.int/catalogue/EO:EUM:DAT:0617, last access: 2024-10-17, 2019b.

Forster, L. and Mayer, B.: Ice crystal characterization in cirrus clouds III: Retrieval of ice crystal shape and roughness from observations of halo displays, Atmospheric Chemistry and PhysicsAtmos. Chem. Phys., 22, 15 179–15 205, https://doi.org/10.5194/acp-22-15179-2022, 2022.

Fu, Q.: An accurate parameterization of the solar radiative properties of cirrus clouds for climate models, Journal of climateJ. Climate, 9, 2058–2082, https://doi.org/10.1175/1520-0442(1996)009<2058:AAPOTS>2.0.CO;2, 1996.

Fu, Q., Yang, P., and Sun, W.: An accurate parameterization of the infrared radiative properties of cirrus clouds for climate models, Journal of climateJ. Climate, 11, 2223–2237, https://doi.org/10.1175/1520-0442(1998)011<2223:AAPOTI>2.0.CO;2, 1998.

Gasteiger, J., Emde, C., Mayer, B., Buras, R., Buehler, S., and Lemke, O.: Representative wavelengths absorption parameterization applied to satellite channels and spectral bands, Journal of Quantitative Spectroscopy and Radiative TransferJ. Quant. Spectrosc. Ra., 148, 99–115, https://doi.org/10.1016/j.jqsrt.2014.06.024, 2014.

Gettelman, A., Chen, C.-C., and Bardeen, C. G.: The climate impact of COVID-19-induced contrail changes, Atmospheric Chemistry and PhysicsAtmos. Chem. Phys, 21, 9405–9416, https://doi.org/10.5194/acp-21-9405-2021, 2021.

Gierens, K. M. and Vázquez-Navarro, M.: Statistical analysis of contrail lifetimes from a satellite perspective, Meteorologische Zeitschrift, 2018.

Eleftheratos]gierens2008review Gierens, K. M., Lim, L. , and Eleftheratos, K.: A review of various strategies for contrail avoidance, Open Atmospheric Science Journal, 2Meteorol. Z., 1–7, 2008. https://doi.org/10.1127/metz/2018/0888, 2018.

Graf, K., Schumann, U., Mannstein, H., and Mayer, B.: Aviation induced diurnal North Atlantic cirrus cover cycle, Geophysical Research LettersGeophys. Res. Lett., 39, https://doi.org/10.1029/2012GL052590, 2012.

Haywood, J. M., Allan, R. P., Bornemann, J., Forster, P. M., Francis, P. N., Milton, S., Rädel, G., Rap, A., Shine, K. P., and Thorpe, R.: A case study of the radiative forcing of persistent contrails evolving into contrail-induced cirrus, Journal of Geophysical Research: AtmospheresJ. Geophys. Res.-Atmos., 114, https://doi.org/10.1029/2009JD012650, 2009, 2009.

Heintzenberg, J. and Charlson, R. J.: Cloud-controlling factors of cirrus, 2009.

Hoese, D.: SatPy: A Python Library for Weather Satellite Processinglibrary for weather satellite processing, in: 99th American Meteorological Society Annual Meeting, AMSAmerican Meteorological Society, 2019.

Howitt, O. J., Carruthers, M. A., Smith, I. J., and Rodger, C. J.: Carbon dioxide emissions from international air freight, ~~Atmospheric Environment~~Atmos. Environ., 45, 7036–7045, https://doi.org/10.1016/j.atmosenv.2011.09.051, 2011.

Hu, Y. and Stamnes, K.: An accurate parameterization of the radiative properties of water clouds suitable for use in climate models, ~~Journal of climate~~J. Climate, 6, 728–742, https://doi.org/10.1175/1520-0442(1993)006<0728:AAPOTR>2.0.CO;2, 1993.

Huckle, R. and Fischer, R. P. D. H.: Determination of clouds in MSG data for the validation of clouds in a regional climate model, Ph.D. thesis, Verlag nicht ermittelbar, 2009.

IPCC, ed.: Climate Change 2023: Synthesis Report. Contribution of Working Groups I, II and III to the Sixth Assessment Report of the Intergovernmental Panel on Climate Change, IPCC, Geneva, Switzerland, available at: https://www.ipcc.ch/report/sixth-assessment-report-synthesis-report/, 2023.

Järvinen, E., Jourdan, O., Neubauer, D., Yao, B., Liu, C., Andreae, M. O., Lohmann, U., Wendisch, M., McFarquhar, G. M., Leisner, T., et al.: Additional global climate cooling by clouds due to ice crystal complexity, ~~Atmospheric Chemistry and Physics~~Atmos. Chem. Phys., 18, 15 767–15 781, https://doi.org/10.5194/acp-18-15767-2018, 2018.

Ji-Cheng, H. and Yu-Qing, X.: Estimation of the aircraft CO2 emissions of China's civil aviation during 1960–2009, ~~Advances in Climate Change Research~~Adv. Clim. Chang. Res., 3, 99–105, https://doi.org/10.3724/SP.J.1248.2012.00099, 2012.

Kärcher, B. and Burkhardt, U.: Effects of optical depth variability on contrail radiative forcing, Quarterly Journal of the Royal Meteorological Society, 139, 1658–1664, 2013.

Kärcher, B., Mayer, B., Gierens, K., Burkhardt, U., Mannstein, H., and Chatterjee, R.: Aerodynamic contrails: Microphysics and optical properties, Journal of the atmospheric sciences, 66, 227–243, 2009.

Lee, D. S., Fahey, D. W., Forster, P. M., Newton, P. J., Wit, R. C., Lim, L. L., Owen, B., and Sausen, R.: Aviation and global climate change in the 21st century, ~~Atmospheric environment~~Atmos. Environ., 43, 3520–3537, https://doi.org/10.1016/j.atmosenv.2009.04.024, 2009.

Lee, D. S., Fahey, D. W., Skowron, A., Allen, M. R., Burkhardt, U., Chen, Q., Doherty, S. J., Freeman, S., Forster, P. M., Fuglestvedt, J., et al.: The contribution of global aviation to anthropogenic climate forcing for 2000 to 2018, ~~Atmospheric environment~~Atmos. Environ., 244, 117 834, https://doi.org/10.1016/j.atmosenv.2020.117834, 2021.

~~Lee, H., Calvin, K., Dasgupta, D., Krinner, G., Mukherji, A., Thorne, P., Trisos, C., Romero, J., Aldunce, P., Barrett, K., et al.: Climate change 2023: synthesis report. Contribution of working groups I, II and III to the sixth assessment report of the intergovernmental panel on climate change, The Australian National University, 2023.~~

Letcher, T. M.: Introduction with a focus on atmospheric carbon dioxide and climate change, ~~in: Future energy, pp. 3–17, Elsevier~~https://doi.org/10.1016/B978-0-08-102886-5.00001-3, 2020.

Mannstein, H. and Schumann, U.: Aircraft induced contrail cirrus over Europe, ~~Meteorologische Zeitschrift~~Meteorol. Z., 14, 549–554, https://doi.org/10.1127/0941-2948/2005/0058, 2005.

~~Mannstein, H., Meyer, R. , and Wendling, P.: Operational detection of contrails from NOAA-AVHRR-data, International Journal of Remote Sensing, 20, 1641–1660, 1999.~~

Markowicz, K. M. and Witek, M.: Sensitivity study of global contrail radiative forcing due to particle shape, Journal of Geophysical Research: Atmospheres, 116, 2011.

Mayor, K. and Tol, R. S.: Scenarios of carbon dioxide emissions from aviation, ~~Global Environmental Change~~Sci. Tech., 20, 65–73, https://doi.org/10.1016/j.gloenvcha.2009.08.001, 2010.

Mecikalski, J. R., Watts, P. D., and Koenig, M.: Use of Meteosat Second Generation optimal cloud analysis fields for understanding physical attributes of growing cumulus clouds, ~~Atmospheric Research~~Atmos. Res., 102, 175–190, https://doi.org/10.1016/j.atmosres.2011.06.023 Get rights and content, 2011.

Meijer, V. R., Kulik, L., Eastham, S. D., Allroggen, F., Speth, R. L., Karaman, S., and Barrett, S. R.: Contrail coverage over the United States before and during the COVID-19 pandemic, ~~Environmental Research Letters~~Environ. Res. Lett., 17, 034 039, https://doi.org/10.1088/1748-9326/ac26f0, 2022.

NASA, A. S. D. C. A.: Single Scanner Footprint TOA/Surface Fluxes and Clouds (SSF), https://ceres.larc.nasa.gov/documents/DPC/DPC_current/pdfs/DPC_SSF-Ed4_R5V1.pdf, 2019.

Olsthoorn, X.: Carbon dioxide emissions from international aviation: 1950–2050, ~~Journal of AirTransport Management~~J. Air. Transp. Manag., 7, 87–93, https://doi.org/10.1016/S0969-6997(00)00031-4, 2001.

Ortiz, I., Dimitropoulou, E., de Buyl, P., Clerbaux, N., García-Heras, J., Jafarimoghaddam, A., Brenot, H., van Gent, J., Sievers, K., Otero, E., et al.: Satellite-Based Quantification of Contrail Radiative Forcing over Europe: A Two-Week Analysis of Aviation-Induced Climate Effects, ~~arXiv preprint arXiv:2409.10166~~https://doi.org/10.48550/arXiv.2409.10166, 2024.

Ortiz, I., García-Heras, J., Jafarimoghaddam, A., and Soler, M.: Enhancing GOES-16 Contrail Segmentation through Ensemble Neural Network Modeling and Optical Flow Corrections, ~~Authorea Preprints~~IEEE T. Geosci. Remote (Under review), https://doi.org/10.36227/techrxiv.173749955.56653418/v1, 2025.

Pejovic, T., Noland, R. B., Williams, V., and Toumi, R.: Estimates of UK CO 2 emissions from aviation using air traffic data, Climatic change, 88, 367–384, https://doi.org/10.1007/s10584-007-9370-0, 2008.

Rädel, G. and Shine, K. P.: Radiative forcing by persistent contrails and its dependence on cruise altitudes, ~~Journal of Geophysical Research: Atmospheres~~J. Geophys. Res.-Atmos., 113, https://doi.org/10.1029/2007JD009117, 2008.

Roberto, N.: Satellite analysis of cloud characteristics at different temporal and spatial scales using visible and infrared wavelengths., 2010.

Rodgers, C. D.: Inverse ~~methods for atmospheric sounding: theory and practice, vol. 2, World scientific~~Methods for Atmospheric Sounding: Theory and Practice, World Scientific, River Edge, USA, 2000.

Sanz-Morère, I., Eastham, S. D., Speth, R. L., and Barrett, S. R.: Reducing uncertainty in contrail radiative forcing resulting from uncertainty in ice crystal properties, ~~Environmental Science & Technology Letters~~Environ. Sci. Tech. Let., 7, 371–375, https://doi.org/10.1021/acs.estlett.0c00150, 2020.

Schmetz, J., Pili, P., Tjemkes, S., Just, D., Kerkmann, J., Rota, S., and Ratier, A.: An introduction to Meteosat second generation (MSG), ~~Bulletin of the American Meteorological Society~~B. Am. Meteorol. Soc., 83, 977–992, https://doi.org/10.1175/1520-0477(2002)083<0977:AITMSG>2.3.CO;2, 2002.

Schumann, U.: Formation, properties and climatic effects of contrails, Comptes Rendus Physique, 6, 549–565, 2005.

Schumann, U. and Graf, K.: Aviation-induced cirrus and radiation changes at diurnal timescales, ~~Journal of Geophysical Research: Atmospheres~~J. Geophys. Res., 118, 2404–2421, https://doi.org/10.1002/jgrd.50184, 2013.

Schumann, U. and Mayer, B.: Sensitivity of surface temperature to radiative forcing by contrail cirrus in a radiative-mixing model, Atmos. Chem. Phys., 17, 13 833–13 848, https://doi.org/10.5194/acp-17-13833-2017, 2017.

Schumann, U., Baumann, R., Baumgardner, D., Bedka, S. T., Duda, D. P., Freudenthaler, V., Gayet, J.-F., Heymsfield, A. J., Minnis, P., Quante, M., et al.: Properties of individual contrails: a compilation of observations and some comparisons, ~~Atmospheric Chemistry and Physics~~Atmos. Chem. Phys., 17, 403–438, https://doi.org/10.5194/acp-17-403-2017, 2017.

Spangenberg

Schumann, W., Stark, H., McMullan, K., Aminou, D. A., Minnis, P. , Bedka, S. T., Palikonda, and Luhmann, H.: The MSG system, ESA bulletin, pp. 11–14, 2002.

Smith, C. J., Kramer, R., Duda, D. J., Myhre, G., Alterskjær, K., Collins, W., Sima, A., Boucher, O., Dufresne, J.-L., Nabat, P., and Rose, F. G.: Contrail radiative forcing over the Northern Hemisphere from 2006 Aqua MODIS data, Geophysical Research Letters, 40, 595–600, 2013. Michou, M., et al.: Effective radiative forcing and adjustments in CMIP6 models, Atmos. Chem. Phys., 20, 9591–9618, https://doi.org/10.5194/acp-20-9591-2020, 2020.

Stamnes, K., Tsay, S.-C., Wiscombe, W., and Laszlo, I.: DISORT, a general-purpose Fortran program for discrete-ordinate-method radiative transfer in scattering and emitting layered media: documentation of methodologyGeneral-Purpose Fortran Program for Discrete-Ordinate-Method Radiative Transfer in Scattering and Emitting Layered Media: Documentation of Methodology, Tech. rep., Dept. of Physics and Engineering Physics, Stevens Institute of Technology, 2000.

Stephens, G. L., Tsay, S.-C., Stackhouse Jr, P. W., and Flatau, P. J.: The relevance of the microphysical and radiative properties of cirrus clouds to climate and climatic feedback, Journal of J. Atmos. Sci., 47, 1742–1754, https://doi.org/10.1175/1520-0469(1990)047<1742:TROTMA>2.0.CO;2, 1990.

Stephens, G. L., Wood, N. B., and Gabriel, P. M.: An assessment of the parameterization of subgrid-scale cloud effects on radiative transfer. Part I: Vertical overlap, Journal of the atmospheric sciences, 47, 1742–1754, 1990. 61, 715–732, 2004.

Teoh, R., Engberg, Z., Schumann, U., Voigt, C., Shapiro, M., Rohs, S., and Stettler, M.: Global aviation contrail climate effects from 2019 to 2021, EGUsphere, 2023, 1–32, 2023. Atmos. Chem. Phys., 24, 6071—6093, https://doi.org/10.5194/acp-24-6071-2024, 2024.

Unterstrasser, S.: Properties of young contrails–a parametrisation based on large-eddy simulations, Atmospheric Chemistry and PhysicsAtmos. Chem. Phys., 16, 2059–2082, https://doi.org/10.5194/acp-16-2059-2016, 2016.

Unterstrasser, S.: The contrail mitigation potential of aircraft formation flight derived from high-resolution simulations, Aerospace, 7, 170, https://doi.org/10.3390/aerospace7120170, 2020.

Wang, X., Wolf, K., Boucher, O., and Bellouin, N.: Radiative effect of two contrail cirrus outbreaks over Western Europe estimated using geostationary satellite observations and radiative transfer calculations, Geophysical Research LettersGeophys. Res. Lett., 51, e2024GL108 452, https://doi.org/10.1029/2024GL108452, 2024.

Wang, Z., Bugliaro, L., Jurkat-Witschas, T., Heller, R., Burkhardt, U., Ziereis, H., Dekoutsidis, G., Wirth, M., Groß, S., Kirschler, S., et al.: Observations of microphysical properties and radiative effects of a contrail cirrus outbreak over the North Atlantic, Atmospheric Chemistry and PhysicsAtmos. Chem. Phys., 23, 1941–1961, https://doi.org/10.5194/acp-23-1941-2023, 2023.

Watts, P., Bennartz, R., and Fell, F.: Retrieval of two-layer cloud properties from multispectral observations using optimal estimation, Journal of Geophysical Research: AtmospheresJ. Geophys. Res.-Atmos., 116, https://doi.org/10.1029/2011JD015883, 2011.

Wielicki, B. A., Cess, R. D., King, M. D., Randall, D. A., and Harrison, E. F.: Mission to planet Earth: Role of clouds and radiation in climate, Bulletin of the American Meteorological SocietyB. Am. Meteorol. Soc., pp. 2125–2153, https://doi.org/10.1175/1520-0477(1995)076<2125:MTPERO>2.0.CO;2, 1995.

Wolf, K., Bellouin, N., and Boucher, O.: Sensitivity of cirrus and contrail radiative effect on cloud microphysical and environmental parameters, Atmospheric Chemistry and PhysicsAtmos. Chem. Phys., 23, 14 003–14 037, https://doi.org/10.5194/acp-23-14003-2023, 2023.

Yang, P., Bi, L., Baum, B. A., Liou, K.-N., Kattawar, G. W., Mishchenko, M. I., and Cole, B.: Spectrally consistent scattering, absorption, and polarization properties of atmospheric ice crystals at wavelengths from 0.2 to 100 μm, ~~Journal of the atmospheric sciences~~J. Atmos. Sci., 70, 330–347, https://doi.org/10.1175/JAS-D-12-039.1, 2013.